

Anomalous grain dynamics and grain locomotion of odd crystals

Zhi-Feng Huang,¹ Michael te Vrugt,² Raphael Wittkowski,³ and Hartmut Löwen⁴

¹*Department of Physics and Astronomy, Wayne State University, Detroit, Michigan 48201, USA*

²*Institut für Physik, Johannes Gutenberg-Universität Mainz, 55128 Mainz, Germany*

³*Department of Physics, RWTH Aachen University; DWI – Leibniz Institute for Interactive Materials; 52074 Aachen, Germany*

⁴*Institut für Theoretische Physik II: Weiche Materie, Heinrich-Heine-Universität Düsseldorf, 40225 Düsseldorf, Germany*

Crystalline or polycrystalline systems governed by odd elastic responses are known to exhibit complex dynamical behaviors involving self-propelled dynamics of topological defects with spontaneous self-rotation of chiral crystallites. Unveiling and controlling the underlying mechanisms require studies across multiple scales. We develop such a type of approach that bridges between microscopic and mesoscopic scales, in the form of a phase field crystal model incorporating transverse interactions. This continuum density field theory features two-dimensional parity symmetry breaking and odd elasticity, and generates a variety of interesting phenomena that agree well with recent experiments and particle-based simulations of active and living chiral crystals, including self-rotating crystallites, dislocation self-propulsion and proliferation, and fragmentation in polycrystals. We identify a distinct type of surface cusp instability induced by self-generated surface odd stress that results in self-fission of single-crystalline grains. This mechanism is pivotal for the occurrence of various anomalous grain dynamics for odd crystals, particularly the predictions of a transition from normal to reverse Ostwald ripening for self-rotating odd grains, and a transition from grain coarsening to grain self-fragmentation in the dynamical polycrystalline state with an increase of transverse interaction strength. We also demonstrate that the single-grain dynamics can be maneuvered through the variation of interparticle transverse interactions. This allows to steer the desired pathway of grain locomotion and to control the transition between grain self-rotation, self-rolling, and self-translation. Our results provide insights for the design and control of structural and dynamical properties of active odd elastic materials.

The understanding and control of grain growth dynamics are among the key subjects in the study of crystalline and polycrystalline materials. Typical phenomena include the classical process of Ostwald ripening [1], which corresponds to the growth of larger grains at the expense of vanishing smaller ones via intergrain particle diffusion through the liquid medium, and the dynamics of grain coarsening in polycrystals, for which the evolution of topological defects, particularly grain boundaries and dislocations, plays a crucial role [2, 3]. Most of the conventional passive materials are potential systems, where microscopically the interparticle interactions are governed by center-center longitudinal forces and the corresponding interaction potentials, while mesoscopically and macroscopically the system evolution and grain dynamics are driven by the pathways towards the equilibrium state characterized by minimum free energy of the system. However, this principle of thermodynamic-potential minimization can no longer be applied for active systems, particularly when the microscopic interactions involve nonconservative transverse forces oriented perpendicularly to the center-center direction of the two interacting active bodies (as originated from, e.g., hydrodynamic near-field interactions between spinning particles [4–8]). This can lead to the existence of nonreciprocal torques between two active particles; the resulting many-body systems are nonpotential and intrinsically nonequilibrium.

Although in the bulk state of a perfect crystalline lattice, all the interparticle transverse forces are balanced and

would not affect the crystal stability, small deformations will lead to odd elastic responses, as identified in continuum odd elasticity theory [9], with antisymmetric or odd elastic constant tensor $C_{ijkl}^{(o)} = -C_{klij}^{(o)}$ and asymmetric stress $\sigma_{ij} \neq \sigma_{ji}$ showing nonzero internal torque caused by transverse forces and the lack of angular momentum conservation. This results in the self-generated dynamics of topological defects inside crystalline grains and the self-rotation of odd crystallites induced by nonzero net odd stress and torque on surface, as observed in both experiments [6–8] and simulations [6–8, 10–12] of various active and living chiral crystals formed by, e.g., swimming bacteria [6], starfish embryos [7], and magnetic colloids [8]. More complex behaviors occur for large-scale odd polycrystalline systems activated by persistent dynamics of motile defects, such as the self-kneading polycrystal whorl state found in recent magnetic colloidal experiments [8].

Such chiral odd crystalline systems naturally involve multiple spatial and temporal scales that mutually couple, in particular microscopic scales at the individual particle or discrete-lattice level and mesoscopic scales of structural patterns or interfacial profiles across, e.g., solid-liquid or grain boundaries. However, current theoretical and computational studies of odd elastic systems mostly focus on two ends of the scaling spectrum, i.e., discrete particle-based simulations [6–8, 10–14] by which only limited length and time scales can be accessed, and continuum elasticity theory [9, 10, 15] for the description of long-wavelength behaviors of the system but with the ab-

sence of microscopic crystalline symmetry and structures. Although continuum field theories have been developed for the study of nonreciprocal active matter, including nonreciprocal coupling between different species [16–21] and nonreciprocal interactions within a single species [22, 23], what has been still lacking is a truly multiscale approach which incorporates the coupling and bridging between microscopic/discrete and mesoscopic/continuum scales for the modeling of odd crystalline or polycrystalline systems. This hinders our efforts on further examining and predicting the complex dynamical behavior of odd grains with elastic or plastic deformations.

Here we develop such a micro- and meso-scale approach based on the phase field crystal (PFC) method which incorporates discrete crystalline structure into continuum density field theory and well captures the system elasticity, plasticity, and multigrain dynamics [24–30], as has been demonstrated through its wide range of applications in solid, soft, and active systems [31–41]. Effects of transverse interactions are introduced into this continuum field model as nonpotential contributions through derivation from microscopic particle dynamics, leading to a new PFC model incorporating transverse interactions (T-PFC model) and the corresponding mesoscale amplitude equation formulation. The modeling reveals a number of intriguing properties of two-dimensional (2D) odd elastic crystals and grains involving complex dynamics of topological defects, with the underlying mechanisms elucidated via the development of a new type of surface cusp instability that leads to grain self-fission through dislocation proliferation. The model predictions also include three types of transitions for odd grain dynamics, namely a transition from normal to reverse Ostwald ripening, a transition between the traditional behavior of grain coarsening and the persistent grain self-fragmentation in the dynamical polycrystalline state, and in terms of grain locomotion, the controlled transition from self-rotation to self-rolling (a combination of self-rotation and translation) and to self-translation of grains. Our results are not only consistent with existing experiments and particle-based or molecular dynamics (MD) simulations of various active and living chiral crystalline systems, but also predict novel mechanisms and conditions that are applicable and extendable to the further study of chiral material systems with odd elastic response.

MODEL

Based on the PFC approach, we represent the spatiotemporal distribution of particles by a local particle density variation field $\psi(\mathbf{r}, t)$. Contributions from longitudinal interactions are described by the PFC free energy functional $F_{\text{PFC}} = \int d\mathbf{r} \{ \frac{1}{2} \psi [-\epsilon + (\nabla^2 + q_0^2)^2] \psi - \frac{1}{3} g \psi^3 + \frac{1}{4} \psi^4 \}$, where the rescaled model parameters ϵ and g can be expressed via the Fourier components of interparticle direct

correlation functions [25, 42], and $q_0 = 1$ after rescaling by choosing the lattice spacing of the crystalline phase as a length scale. The corresponding flux is given by $\mathbf{J}_{\text{PFC}} = -\nabla \mu_{\text{PFC}} = -\nabla \delta F_{\text{PFC}} / \delta \psi$, where μ_{PFC} is the chemical potential. The transition and coexistence between solid and liquid (homogeneous) states are determined by ϵ and the average density $\bar{\psi}_0$. Here, we incorporate the nonpotential contribution by coarse-graining the microscopic equations of motion of particles interacting via a transverse force $\mathbf{F}_{ab}^\perp = f^\perp(\mathbf{r}_a, \mathbf{r}_b) \hat{\mathbf{r}}_{ab}^\perp$ between any two particles a and b , with $\hat{\mathbf{r}}_{ab}^\perp = \hat{\mathbf{z}} \times \hat{\mathbf{r}}_{ab}$, $\hat{\mathbf{z}}$ the out-of-plane unit vector, and $\hat{\mathbf{r}}_{ab} = (\mathbf{r}_a - \mathbf{r}_b) / |\mathbf{r}_a - \mathbf{r}_b|$. Details of the derivation are given in SI Appendix. The nonpotential flux is found to be

$$J_{T,i} = -\psi (\alpha_0 + \alpha_1 \nabla^2 + \alpha_2 \nabla^4) \epsilon_{ij} \partial_j \psi, \quad (1)$$

where $i, j = x, y$, ϵ_{ij} is the 2D Levi-Civita symbol, and α_k ($k = 0, 1, 2$) are proportional to the strength of transverse interaction (with expressions determined by the specific form of transverse force f^\perp). Here we allow the coefficients α_k to vary with space and/or time. The term proportional to α_1 is consistent with one found in the chiral current of a different type of chiral active matter, namely circle swimmers [43].

The dynamics of the density field is then governed by $\partial \psi / \partial t = -\nabla \cdot \mathbf{J} = -\nabla \cdot (\mathbf{J}_T + \mathbf{J}_{\text{PFC}})$ with a diffusive timescale, giving the T-PFC model equation

$$\begin{aligned} \frac{\partial \psi}{\partial t} = & [\nabla (\alpha_0 \psi) \times \nabla \psi + \nabla (\alpha_1 \psi) \times \nabla \nabla^2 \psi \\ & + \nabla (\alpha_2 \psi) \times \nabla \nabla^4 \psi]_z + \nabla^2 \frac{\delta F_{\text{PFC}}}{\delta \psi}. \end{aligned} \quad (2)$$

For spatially and temporally constant coefficients α_k , the T-PFC equation 2 reduces to

$$\begin{aligned} \frac{\partial \psi}{\partial t} = & [(\nabla \psi) \times \nabla (\alpha_1 \nabla^2 \psi + \alpha_2 \nabla^4 \psi)]_z \\ & + \nabla^2 [-\epsilon \psi + (\nabla^2 + q_0^2)^2 \psi - g \psi^2 + \psi^3]. \end{aligned} \quad (3)$$

The first term of Eq. 3, originating from transverse interaction, breaks the 2D parity symmetry, which can then lead to 2D chirality. It is also antisymmetric with respect to the exchange of x and y , resulting in a non-Hermitian dynamical matrix for the elastodynamics of the displacement field, a characteristic of nonreciprocity (see SI Appendix). In addition, it is straightforward to prove that this 2D T-PFC equation is rotationally invariant with respect to a rotation about the z axis, i.e., maintaining global rotational invariance in 2D, in addition to translational invariance.

Amplitude Expansion

The mesoscale description of the model is obtained from the corresponding amplitude expansion, i.e.,

$$\psi = \psi_0 + \sum_{j=1}^3 A_j e^{i\mathbf{q}_j^0 \cdot \mathbf{r}} + \text{c.c.}, \quad (4)$$

where $\mathbf{q}_1^0 = \tilde{q}_0(-\frac{\sqrt{3}}{2}\hat{\mathbf{x}} - \frac{1}{2}\hat{\mathbf{y}})$, $\mathbf{q}_2^0 = \tilde{q}_0\hat{\mathbf{y}}$, and $\mathbf{q}_3^0 = \tilde{q}_0(\frac{\sqrt{3}}{2}\hat{\mathbf{x}} - \frac{1}{2}\hat{\mathbf{y}})$ are the basic wave vectors of a 2D hexagonal lattice, with $\hat{\mathbf{x}}$ and $\hat{\mathbf{y}}$ the unit vectors along the x and y directions respectively, and \tilde{q}_0 ($\sim q_0$) is the steady-state selected wave number. The 0th-mode average density field ψ_0 and the complex amplitude A_j ($j = 1, 2, 3$) vary at the mesoscopic “slow” scales. Substituting Eq. 4 into Eq. 3 and following the procedure of amplitude equation formulation [42, 44] by separating microscopic and mesoscopic scales, we get

$$\begin{aligned} \frac{\partial \psi_0}{\partial t} = & [(\nabla \psi_0) \times \nabla (\alpha_1 \nabla^2 \psi_0 + \alpha_2 \nabla^4 \psi_0)]_z \\ & + \sum_j \{ [(\nabla + i\mathbf{q}_j^0) A_j] \times (\nabla - i\mathbf{q}_j^0) \}_z \\ & \times \mathcal{L}_j^* (\alpha_1 + \alpha_2 \mathcal{L}_j^*) A_j^* + \text{c.c.} + \nabla^2 \frac{\delta \mathcal{F}_{\text{PFC}}}{\delta \psi_0}, \end{aligned} \quad (5)$$

$$\begin{aligned} \frac{\partial A_j}{\partial t} = & [(\nabla \psi_0) \times (\nabla + i\mathbf{q}_j^0)]_z \mathcal{L}_j (\alpha_1 + \alpha_2 \mathcal{L}_j) A_j \\ & + \{ [(\nabla + i\mathbf{q}_j^0) A_j] \times \nabla (\alpha_1 \nabla^2 \psi_0 + \alpha_2 \nabla^4 \psi_0) \}_z \\ & + \sum_{l \neq k \neq j} \{ [(\nabla - i\mathbf{q}_l^0) A_l^*] \times (\nabla - i\mathbf{q}_k^0) \}_z \\ & \times \mathcal{L}_k^* (\alpha_1 + \alpha_2 \mathcal{L}_k^*) A_k^* - \tilde{q}_0^2 \frac{\delta \mathcal{F}_{\text{PFC}}}{\delta A_j^*}, \end{aligned} \quad (6)$$

where $\mathcal{L}_j = \nabla^2 + 2i\mathbf{q}_j^0 \cdot \nabla - \tilde{q}_0^2$ and $\mathcal{F}_{\text{PFC}}[A_j, \psi_0]$ is the mesoscale effective free energy functional (see SI Appendix).

One-Mode Approximation for the Bulk State

For a pristine crystalline phase of hexagonal symmetry, $\psi_0 = \bar{\psi}_0$ and $A_j = A_j^0$ ($j = 1, 2, 3$) are constant in the one-mode approximation. Thus the contributions from transverse interaction terms vanish, as seen from Eqs. 5 and 6, and the exact solution of the steady state is given by

$$\begin{aligned} A_j^0 = A_0 = & \frac{1}{15} \left\{ g - 3\bar{\psi}_0 \right. \\ & \left. + \sqrt{(g - 3\bar{\psi}_0)^2 - 15[-\epsilon + (\tilde{q}_0^2 - q_0^2)^2 + 3\bar{\psi}_0^2 - 2g\bar{\psi}_0]} \right\}. \end{aligned} \quad (7)$$

This agrees with the result of the original PFC model without transverse interactions. The one-mode phase diagram for solid and liquid phases [26] is the same as well.

This is consistent with the microscopic picture of a perfect crystalline bulk state where neighboring transverse forces cancel out and thus have a negligible effect on the system stability, unless there exist elastoplastic deformations or interfaces with varying structural amplitudes, as will be addressed below.

Odd Elasticity

For small elastic deformations, the phases of complex amplitudes vary at long wavelength as a result of a displacement field \mathbf{u} , giving $A_j \simeq A_j^0 \exp(-i\mathbf{q}_j^0 \cdot \mathbf{u})$, where $A_j^0 \simeq A_0$ in the steady state with $\psi_0 \simeq \bar{\psi}_0$. From the amplitude equations 5 and 6, we show in SI Appendix that the displacement field $u_{j=x,y}$ satisfies the elastodynamical equation (i.e., the overdamped Cauchy’s equation of motion)

$$\Gamma \frac{\partial u_j}{\partial t} = \partial_i \sigma_{ij} = C_{ijkl} \partial_i \partial_k u_l, \quad (8)$$

where Γ is the drag coefficient, C_{ijkl} represents the elastic constant tensor, and $\sigma_{ij} = C_{ijkl} \partial_k u_l$ is the stress tensor. To lowest order,

$$\begin{aligned} C_{1111} = C_{2222} &= \Gamma \tilde{q}_0^2 (5\tilde{q}_0^2 - 2q_0^2), \\ C_{1122} = C_{2211} &= \Gamma \tilde{q}_0^2 (2q_0^2 - \tilde{q}_0^2), \\ C_{1212} = C_{2121} = C_{1221} = C_{2112} &= \Gamma \tilde{q}_0^2 (3\tilde{q}_0^2 - 2q_0^2), \end{aligned} \quad (9)$$

as in the original PFC model with regular, even elasticity (where $\tilde{q}_0^2 = q_0^2$ and $\Gamma = 3A_0^2$ [45]). The nonzero transverse interactions lead to additional elastic constants C_{iikl} ($k \neq l$) and C_{ijkk} ($i \neq j$), given by

$$\begin{aligned} C_{1112} = C_{1121} &= -\frac{1}{2} \Gamma A_0 \tilde{q}_0^2 (5\alpha_1 - 13\tilde{q}_0^2 \alpha_2), \\ C_{2221} = C_{2212} &= -C_{1112} = -C_{1121}, \\ C_{1211} = -C_{2122} &= \frac{1}{2} \Gamma A_0 \tilde{q}_0^2 (7\alpha_1 - 23\tilde{q}_0^2 \alpha_2), \\ C_{2111} = -C_{1222} &= \frac{3}{2} \Gamma A_0 \tilde{q}_0^2 (\alpha_1 - \tilde{q}_0^2 \alpha_2), \end{aligned} \quad (10)$$

where the right mirror symmetry $C_{iikl} = C_{iilk}$ is still maintained due to global rotational invariance of the system and the lack of coupling to rotational degrees of freedom, while generally the left minor symmetry is broken, i.e., $C_{ijkk} \neq C_{jikl}$, as a result of nonzero internal torque caused by transverse interactions, which leads to $\sigma_{ij} \neq \sigma_{ji}$ (if $i \neq j$) and the breaking of angular momentum conservation. Notably, the major symmetry is no longer obeyed, with $C_{ijkk} \neq C_{kkij}$ and $C_{iikl} \neq C_{klji}$ in Eq. 10, such that the system incorporates both even and odd elasticity, i.e.,

$$C_{iikl} = C_{iikl}^{(e)} + C_{iikl}^{(o)}, \quad C_{ijkk} = C_{ijkk}^{(e)} + C_{ijkk}^{(o)}, \quad (11)$$

consisting of even elasticity components $C_{ijkl}^{(e)} = C_{klij}^{(e)}$ satisfying major symmetry and odd elasticity components $C_{ijkl}^{(o)} = -C_{klij}^{(o)}$ which are antisymmetric and proportional to transverse interaction strength (with expressions determined by Eq. 10 and shown in SI Appendix). The bulk modulus B and shear modulus μ are then given by

$$\begin{aligned} B &= \frac{1}{2} (C_{1111} + C_{1122}) = 2\Gamma\tilde{q}_0^4, \\ \mu &= \frac{1}{2} (C_{1111} - C_{1122}) = \Gamma\tilde{q}_0^2 (3\tilde{q}_0^2 - 2q_0^2). \end{aligned} \quad (12)$$

We can also identify the odd bulk modulus A induced by nonzero internal torque and the odd shear modulus K^o as

$$\begin{aligned} A &= \frac{1}{2} (C_{2111} - C_{1211}) = -\Gamma A_0 \tilde{q}_0^2 (\alpha_1 - 5\tilde{q}_0^2 \alpha_2), \\ K^o &= C_{1112} = -\frac{1}{2} (C_{2111} + C_{1211}) \\ &= -\frac{\Gamma}{2} A_0 \tilde{q}_0^2 (5\alpha_1 - 13\tilde{q}_0^2 \alpha_2). \end{aligned} \quad (13)$$

All these are consistent with continuum odd elasticity theory [9], with elastic constants expressed explicitly in terms of T-PFC parameters.

RESULTS AND DISCUSSION

Model Validation

In addition to the above analytic results which demonstrate that the T-PFC model developed here incorporates key aspects of the system symmetry (and symmetry breaking), chirality, and odd elastic properties, we have conducted numerical simulations to further validate the model, and to provide evidence for the multiscale nature of this approach where particle-scale resolution is still maintained in this continuum field description. Here the T-PFC model equation 3 is solved numerically (Materials and Methods), with the setting of $\alpha_2 = 0$ for a minimal continuum field model incorporating effects of transverse interaction and odd elasticity. (We have also conducted simulations with nonzero α_2 and found no significant differences.) We have reproduced various phenomena of odd and chiral crystals found in experiments and particle-based simulations and matched the results to the microscopic picture of force, with some simulation outcomes illustrated in Fig. 1. These include self-rotation of odd crystallites (Fig. 1 A and B and Movie S1), as a result of nonzero net transverse force (or net odd stress) and thus a net torque on the free surface of a crystallite embedded in a homogeneous or liquid-state medium, consistent with experiments of, e.g., swimming bacteria [6], starfish embryo [7], and magnetic colloid [8] 2D chiral crystals. Also included are the behaviors of dislocation self-propulsion (Fig. 1C), showing as self-glide

of dislocation along the direction of its Burgers vector (Movie S2) which follows the direction of local net transverse force around the dislocation core, unbinding of a dislocation dipole with opposite Burgers vectors and far enough separation (Movie S3) instead of annihilation in regular crystals (Movie S4), and either expanding (Fig. 1D and Movie S5) or shrinking (Movie S6) of circular grain boundary, depending on the direction of Burgers vectors of boundary dislocations. These results of motile dislocation are consistent with those found in magnetic colloidal experiments and particle-based simulations [8, 10, 11], demonstrating that effects at microscopic, lattice scales (that are not accessible in standard continuum approaches) can be well captured in this continuum T-PFC model.

An advantage of PFC modeling is that it allows to simulate the process of dislocation climb, which is difficult to realize in atomistic simulations like MD as the dynamics involves long-range mass diffusion. As shown in Fig. 1E, two dislocations of opposite sign of Burgers vectors, which would climb towards each other and annihilate in regular crystals (Movie S7), travel apart due to self-gliding caused by transverse interaction (Movie S8). Note that in all the calculations presented here, we choose $\alpha_1 > 0$ which corresponds to the case of two-body transverse force along the direction $\hat{\mathbf{r}}_{ab}^\perp = \hat{\mathbf{z}} \times \hat{\mathbf{r}}_{ab}$. This leads to counterclockwise self-rotation of crystallites and the dislocation self-propulsion along the direction of Burgers vector, while choosing $\alpha_1 < 0$ with opposite direction of interparticle transverse force gives equivalent results, although with opposite direction of self-rotation (clockwise) and dislocation self-glide, as verified in our simulations.

We also quantitatively examine the property of self-rotation of single-crystalline grains, for which the grain rotates faster for larger transverse interaction strength α_1 and smaller grain size, consistent with the microscopic picture. Our T-PFC calculations of grain self-rotation frequency ω at different α_1 show the collapse of data into a power law scaling (Fig. 1B)

$$\frac{\omega}{\alpha_1} \sim N^{-s}, \quad (14)$$

with scaling exponent $s = 0.950 \pm 0.005$, where N is the number of particles in the grain. This well agrees with the experimental measurement of rotating starfish embryo clusters [7], giving a close value of exponent $s = 1.03 \pm 0.06$ within the same range of N (see the inset of Fig. 1B). To understand this N^{-1} scaling, consider the overdamped limit with $\zeta_R \omega = \tau_{\text{net}}$, where ζ_R is the rotational friction coefficient that can be estimated as $\zeta_R \propto R^4 \sim N^2$ for a 2D circular grain of radius R (see SI Appendix), and the self-generated net torque on the grain surface $\tau_{\text{net}} = \int_s R dF_{\text{net}}^\perp \propto \oint R \alpha_1 ds \propto \alpha_1 R^2$ (if assuming balanced transverse interactions in the bulk). This leads to $\omega = \tau_{\text{net}}/\zeta_R \propto \alpha_1/R^2 \sim \alpha_1/N$.

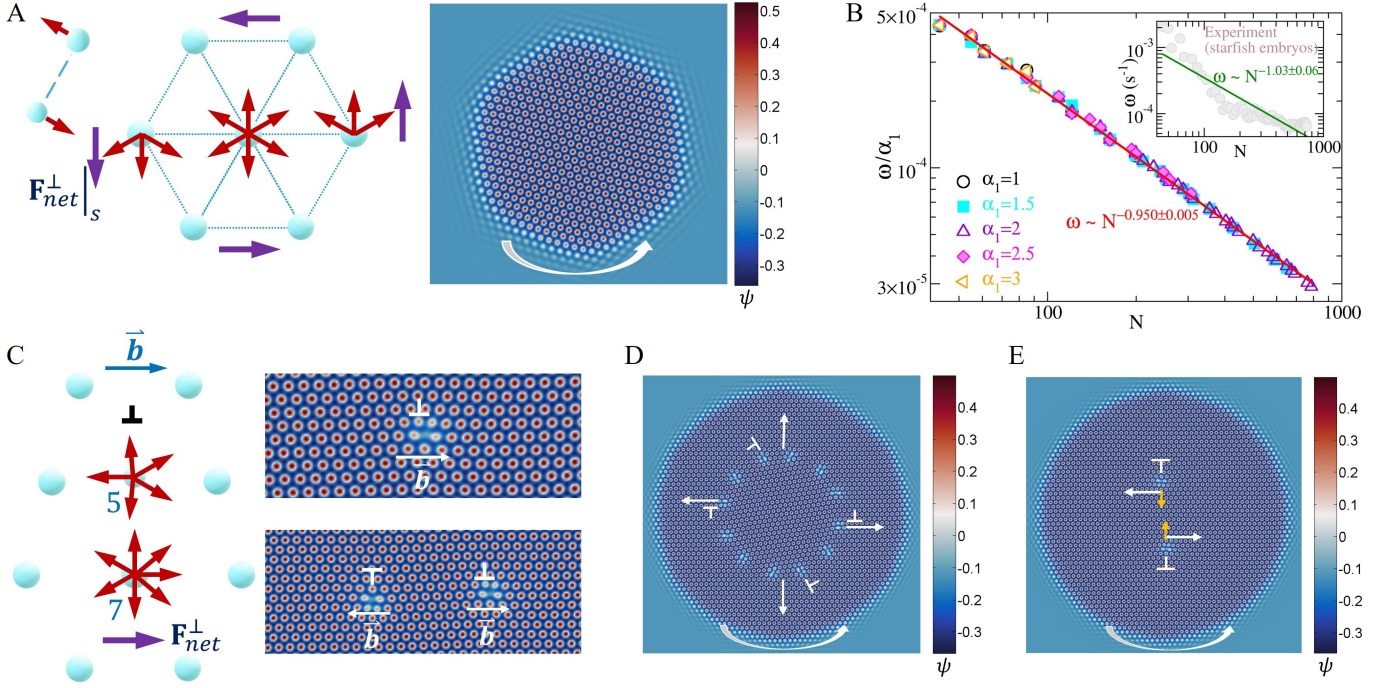


FIG. 1. T-PFC simulation results for self-rotating odd crystals and motile defects. (A) A snapshot of self-rotating single-crystalline grain at $\alpha_1 = 2$, with a schematic illustrating nonzero net transverse force on surface. (B) The scaling of grain rotation frequency ω vs particle number N , showing a data collapse for different transverse interaction strength α_1 . The inset gives the data fitting for experimental results of starfish embryos in Ref. [7] for the same N range. (C) Schematic of a penta-hepta dislocation with local nonzero net transverse force, which leads to dislocation self-glide and the unbinding of a dislocation dipole as shown in the snapshots of simulated ψ profile. The Burgers vector \mathbf{b} is labeled for each dislocation. (D) A self-expanding circular grain boundary within a self-rotating crystallite, with 8° misorientation at $\alpha_1 = 1$. (E) The climb and self-glide of two dislocations of opposite Burgers vectors at $\alpha_1 = 1$. Small arrows indicate the climb direction, and large arrows give the direction of self-glide along the Burgers vectors.

Surface Cusp Instability and Grain Self-Fission

On the free surface of single-crystalline odd grains, the self-generated surface odd stress (with tangential, self-shearing surface net transverse force as illustrated in Fig. 1A) results in the spontaneous development of a new type of surface cusp instability in the absence of any external strain or stress. An example with $\alpha_1 = 2$ is shown in the inset of Fig. 2A and Movie S9. The subsequent nonlinear evolution leads to the nucleation of dislocations at the edges of surface cusps, which self-propel into the bulk as a result of the self-gliding of motile dislocation induced by transverse interaction (Fig. 2B). It occurs beyond a threshold of grain size, characterized by a critical radius R_c which is larger for weaker transverse interaction strength α_1 . A scaling behavior of $R_c \sim |\alpha_1|^{-\beta}$ is identified from our numerical simulations (Fig. 2A), with a scaling exponent $\beta = 2.5 \pm 0.2$.

Note that the odd crystalline system studied here is nonpotential as a result of nonzero transverse interactions, and the system evolution governed by Eq. 3 does not follow the pathway of free energy minimization. Thus this result of grain instability is of nonequilibrium, nonrelax-

ational nature and cannot be identified from energetics arguments used for near-equilibrium potential systems (see SI Appendix for a related calculation). At the later time stage, the continuing process of dislocation proliferation and self-traveling results in a recurring procedure of cracking and self-healing inside the rotating crystallite, yielding internal grain boundary formation and evolution as well as the overall grain distortion (see Movie S9 at $\alpha_1 = 2$). In the case of strong enough transverse interaction, it leads to the occurrence of grain self-fission with self-rotating fragments (Fig. 2C and Movie S10 at $\alpha_1 = 3$). Recent MD simulations and experiments of magnetic colloidal crystals [8] have observed the similar phenomenon of dislocation creation and propulsion from the free boundary of single-crystalline crystallite and the subsequent formation of multidomains and grain boundaries inside the crystallite, although the mechanism of cusp instability and its grain size dependence, as well as the self-division and the resulting grain distortion as found here, were not examined. Thus the mechanism and results identified here are key to understanding those experimental findings. Note also that the phenomena of cusp instability and irregular grain self-fission obtained here for “dry” odd crystals originate from self-generated

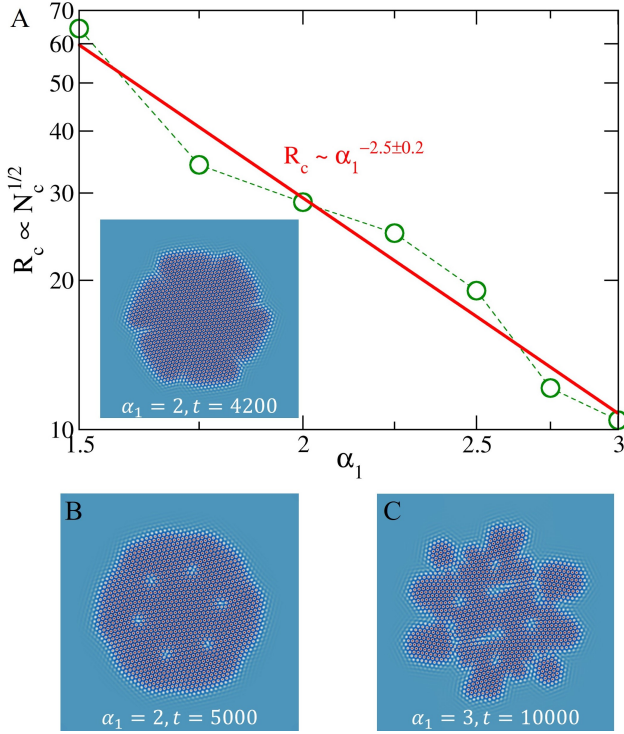


FIG. 2. (A) Critical grain radius R_c for the onset of surface cusp instability as a function of transverse interaction strength α_1 , as identified from T-PFC simulations (up to $t = 10^6$). Snapshots of the ψ profile are shown in the inset of (A) for the instability onset and in (B) for the surface-emitted motile dislocations at $\alpha_1 = 2$, and in (C) for grain self-fission at $\alpha_1 = 3$.

surface odd stresses resulting from transverse interactions, a mechanism that is intrinsically different from the self-shearing instability and hydrodynamic flow-induced splitting of phase-separated fluid droplets found in the “wet” system of Active Model H [46].

Transition from Normal to Reverse Ostwald Ripening

This mechanism of self-stress induced surface instability and the resulting grain self-fission can lead to two phenomena of anomalous multigrain dynamics. The first one is the transition from normal Ostwald ripening to the reverse process with the increase of transverse interaction strength α_1 , for two self-rotating odd crystalline grains. This is demonstrated in Fig. 3A, which shows the time evolution of grain sizes, defined as $L \simeq 2R = 2\sqrt{\mathcal{A}/\pi}$ with grain area \mathcal{A} , at α_1 ranging from 0 (for the original passive PFC model) to 3. The standard process of Ostwald ripening is observed at small enough magnitude of α_1 with zero or weak enough transverse interactions, as expected, for which the initially larger grain with effective radius $R_>(t)$ grows with time after an early time range of relaxation, accompanied by the shrinkage of the initially

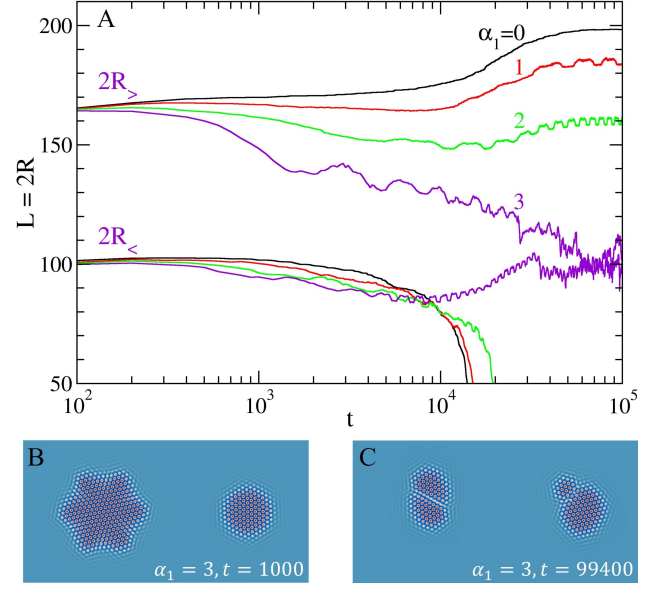


FIG. 3. (A) Time evolution of grain sizes during the ripening process of two crystalline grains, showing a transition from normal to reverse Ostwald ripening with the increase of α_1 . (B and C) Simulation snapshots at $t = 1000$ and 99400 during the process of reverse Ostwald ripening with $\alpha_1 = 3$.

smaller grain with radius $R_<(t)$. At strong enough α_1 , starting from the same initial conditions of grain sizes and spacing, reverse Ostwald ripening occurs when the initial radius $R_<(0)$ of the smaller grain is large enough, showing as the overall decrease of $R_>(t)$ with time and the early-time decrease, slowing-down, and then increase of $R_<(t)$ until both reach a similar scale (Fig. 3 B and C; see also Movie S11 (for $t \leq 20000$) and Movie S12 (for $t = 95000-10^5$), corresponding to the curves of $\alpha_1 = 3$ in Fig. 3A).

This transition can be explained by the behavior of grain self-division and fission. In the case of normal Ostwald ripening, according to the Gibbs-Thomson relation [47] (which has been generalized for the PFC model with the supersaturation of density variation field ψ [48]), i.e., $\delta\mu|_{\text{surface}} \propto \gamma\kappa$ with $\delta\mu = \mu - \mu_{\text{eq}}$, γ the surface tension, and κ the surface curvature, the chemical potential μ and thus particle density at the solid-liquid grain surface increase with the decreasing grain radius (i.e., larger κ), leading to a diffusive mass transport from smaller to larger grains as driven by the local density gradient and consequently, the growth of larger grain at the expense of shrinking and disappearance of smaller grain. This can be changed by strong enough transverse interactions. For a given initial radius $R_>$ of the larger self-rotating grain, when it exceeds the threshold size $R_c(\alpha_1)$, at a high enough α_1 (as quantified in Fig. 2A) a surface cusp instability and the subsequent dislocation proliferation, emission and grain self-fission occur, resulting in smaller fragmented sub-grains and thus the reduced or even re-

versed local density gradient and diffusion flux with respect to the other grain (which has size $R_<$). This leads to the slowing-down, arrest, and reverse of the Ostwald ripening process with the two grains approaching a similar, comparable size, as shown in Fig. 3 (for results of $\alpha_1 = 3$). At the late time stage when the radius of the initially smaller grain $R_<(t) > R_c$, grain self-fission also occurs there, in addition to the self-division of the other grain (Fig. 3C and Movie S12). On the other hand, if the initial $R_<(0)$ is too small, due to the Gibbs-Thomson effect the smaller grain shrinks rapidly and melts before the self-fission and fragmentation of the larger grain take any effect.

This mechanism governing the reverse Ostwald ripening process for odd crystals is thus different from that of phase-separated active fluids caused by negative pseudotension of liquid droplet surface [46, 49], noting the increase of positive γ with stronger transverse interactions (which generate larger tangential surface stress) as found in simulations of chiral fluid interfaces [13]. It is also different from the reverse ripening caused by misfit stress in passive solid systems [50], given the lack of any imposed stress or strain in the system studied here. Hence the transition identified above is a unique feature combining chirality (breaking of 2D parity) and grain self-fission in this odd crystalline system.

Transition from Grain Coarsening to Grain Self-Fragmentation

The second phenomenon originating from the mechanism of surface cusp instability and grain self-fission is the spontaneous formation of a dynamical polycrystalline state during the nucleated growth process, where the system evolves from an initial condition of multiple randomly distributed crystalline nuclei. Examples of system time evolution at small and large α_1 are shown in Movies S13 ($\alpha_1 = 1$) and S14 ($\alpha_1 = 3$), with some simulation snapshots given in Fig. 4, both having the same average density $\bar{\psi}_0 = -0.09$ and starting from the same initial conditions. At the early time stage, a similar behavior is observed in both movies, including the fast growth of nuclei and the impingement and then coalescence of grains, but the subsequent evolution is qualitatively different. At small α_1 (weak transverse interactions), the system dynamics is governed by the motion of topological defects, particularly grain boundaries, similar to the typical process of grain coarsening, although with dislocation self-motion as a result of nonzero transverse force (Fig. 4A and Movie S13). However, for large α_1 (strong transverse interaction), any large enough self-rotating grains, formed after either grain growth or coalescence, exhibit self-fission into smaller parts through dislocation creation on grain surface and propagation across the grain with crack formation. Neighboring rotating grains then

remerge or reheal, self-splitting again if exceeding the instability size threshold (R_c), with the procedure iterated incessantly. This leads to a persistently varying process of grain self-fragmentation instead of coarsening, as seen in Movie S14 and Fig. 4B.

To quantitatively examine this transition from the normal grain coarsening process to the anomalous dynamics of grain fragmentation, we calculate the structure factor $S(\mathbf{q}, t) = |\hat{\psi}_{\mathbf{q}}(t)|^2/V$, with $\hat{\psi}_{\mathbf{q}}(t)$ the Fourier transform of $\psi(\mathbf{r}, t)$ and $V = L_x L_y$ for a 2D system of size $L_x \times L_y$, and the correlation function $C(\mathbf{r}, t) = (\langle \psi(\mathbf{x} + \mathbf{r}, t) \psi(\mathbf{x}, t) \rangle - \bar{\psi}_0^2) / (\langle \psi^2 \rangle - \bar{\psi}_0^2)$ at different times t . The characteristic domain or grain size in the polycrystalline state is identified by two quantities, the correlation length $\xi(t)$ determined via the fitting of the envelope (or peak values) of circularly averaged correlation function to $C_m(r, t) \propto \exp(-r/\xi)$ (Fig. 4D), and domain size $L_1(t) = 2\pi/m_1$ where the first moment $m_1 = \int_0^{q_{m_1}} dq q S(q, t) / \int_0^{q_{m_1}} dq S(q, t)$ is evaluated within the first peak region of small wave numbers $0 < q \leq q_{m_1}$, with q_{m_1} the location of first local minimum of the circularly averaged structure factor $S(q, t)$ (see Fig. 4E, where the other peaks are located at the wave numbers of triangular lattice with ratios $1 : \sqrt{3} : 2$). Note that ξ measures the distance of correlation between local density fluctuations, giving the scale of domains separated by any defects or disorder, while L_1 characterizes the larger-scale profile of solid grains particularly those separated via locally homogeneous or liquid-like boundaries or gaps.

Results of time evolution of the correlation length ξ are presented in Fig. 4F, clearly showing a transition from coarsening-dominated to fragmentation-dominated dynamics with the increase of transverse interaction strength α_1 . A similar behavior is obtained for L_1 from calculations of the first moment. The self-fragmentation state appears earlier for stronger transverse interaction, as characterized by a fluctuating plateau of the average grain size which decreases with larger α_1 as a result of more dynamically fragmented grains. This is consistent with the α_1 -dependence of threshold R_c for grain instability found in Fig. 2A, although with different values of the scaling exponent. The scalings of characteristic domain sizes averaged over a late time stage (e.g., $t = 8 \times 10^4 - 10^5$) are shown in Fig. 4 G and H, giving $\langle \xi \rangle \sim |\alpha_1|^{-\beta_\xi}$ and $\langle L_1 \rangle \sim |\alpha_1|^{-\beta_{m_1}}$ in the fragmentation-dominated regime, with scaling exponents $\beta_\xi = 0.85 \pm 0.02$ and $\beta_{m_1} = 1.718 \pm 0.009$ respectively (similar results are obtained if choosing different late time ranges for averaging or different system sizes). The transition point between regimes of two different grain dynamics can be estimated as the beginning of the scaling regime, which occurs around $\alpha_1 \simeq 1.75$ as identified from Fig. 4 G and H.

This phenomenon of multigrain self-fragmentation dynamics closely resembles the self-kneading polycrystal whorl state observed in recent experiments of magnetic

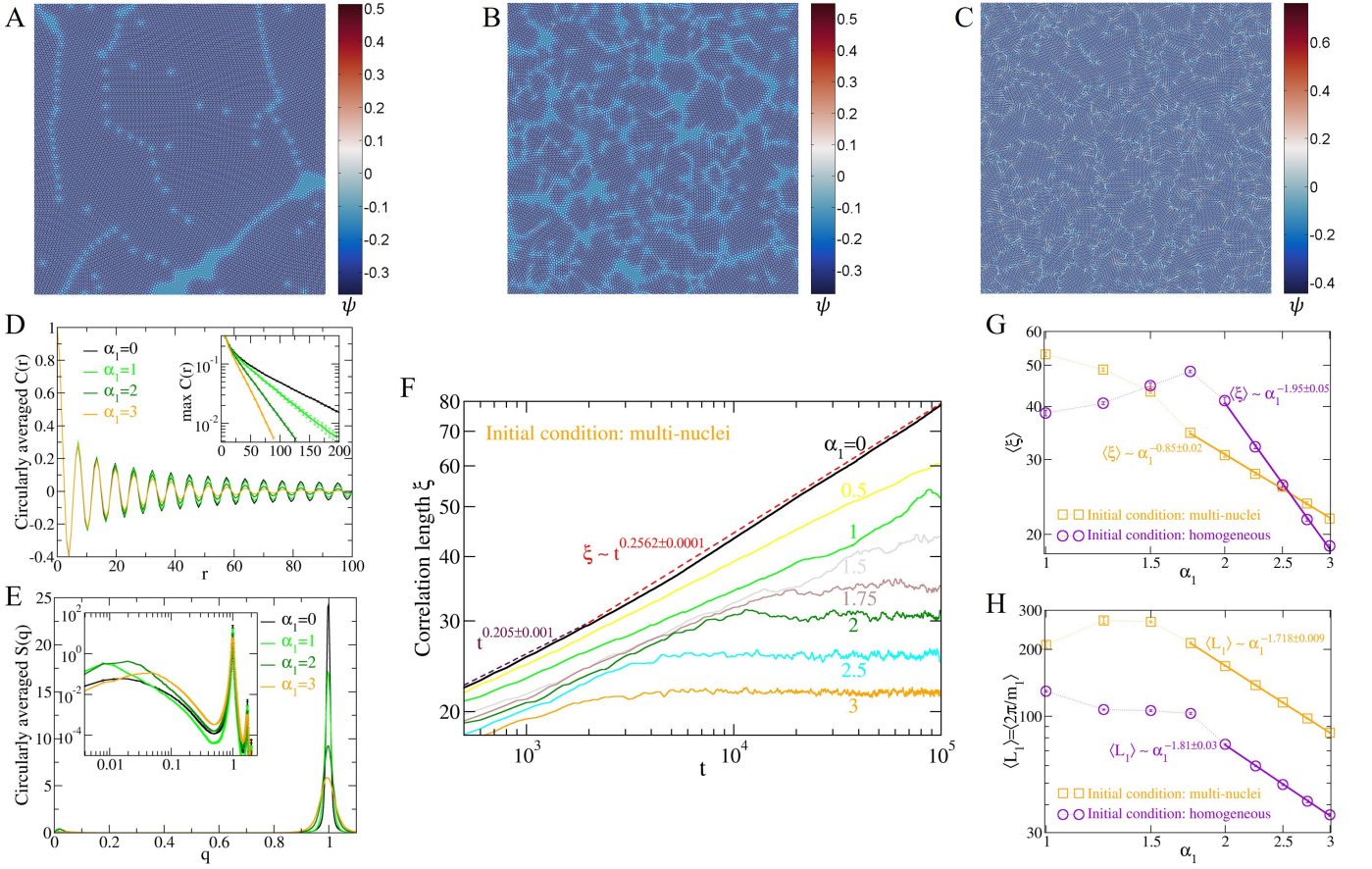


FIG. 4. Multigrain dynamics of the odd polycrystalline state. (A-C) Simulation snapshots at $t = 10^5$, each showing the central quarter of the 2048×2048 simulated system, for initial conditions of multiple crystalline nuclei with $\bar{\psi}_0 = -0.09$ at (A) $\alpha_1 = 1$ governed by grain coarsening dynamics and (B) $\alpha_1 = 3$ governed by grain self-fragmentation, and (C) from homogeneous initial state with $\bar{\psi}_0 = 0$ at $\alpha_1 = 3$. (D) Circularly averaged correlation function $C(r)$, with inset showing the exponential decay of its peak values, and (E) circularly averaged structure factor $S(q)$, with the corresponding log-log plots given in the inset, both at $t = 10^5$ and for initial conditions of multiple nuclei. (F) Time variation of the correlation length ξ , showing a transition from grain coarsening to self-fragmentation dynamics with the increase of transverse interaction strength α_1 . (G and H) $\langle \xi \rangle$ and $\langle L_1 \rangle$, averaged over the late time stage ($t = 8 \times 10^4 - 10^5$), as a function of α_1 , for two types of initial conditions. Power-law scalings are identified in the regime of grain self-fragmentation. Results in (D-H) have been averaged over 20 simulation runs for 2048×2048 system size.

colloidal odd crystals [8], where the average grain size is also found to decrease with stronger transverse interaction at higher colloid spinning frequency. This phenomenon, however, is fundamentally different from the clustering or rotating flocks observed in active chiral fluids composed of spinning colloidal particles [13, 51–53]. There, although a steady state of finite size clusters without coarsening can form at high enough spinning rates, each of self-rotating clusters or flocks is in the liquid phase with the presence of edge current [13, 53] but without the mechanism of surface instability or grain self-fission found in the odd crystals studied here.

In the above study of multigrain dynamics, the average density of the system ($\bar{\psi}_0 = -0.09$) is chosen such that some small liquid-state regions or gaps can coexist with solid grains, facilitating the occurrence of grain surface instability. Our simulations indicate that the grain

boundaries themselves, without any surrounding liquid, can also develop an instability and emit motile dislocations, causing self-fission of grains. We thus simulate systems of pure solid phase with high enough average density ($\bar{\psi}_0 = 0$), starting from initial conditions of spatially homogeneous phase. A polycrystalline state emerges spontaneously, with differently oriented domains separated by grain boundaries and dislocations. Similarly, the subsequent evolution is governed by two distinct types of dynamics, grain coarsening at weak transverse interaction strength α_1 , and as α_1 increases, a transition to the persistent dynamical state of grain self-fragmentation (Movie S15 and Fig. 4C), although with a different morphology of self-rotating fragmented multigrains. Such a transition occurs at the similar magnitude of α_1 , around $\alpha_1 \simeq 2$ as obtained from Fig. 4 G and H. It also features the power-law scalings of $\langle \xi \rangle$ and $\langle L_1 \rangle$, but with much larger

exponents $\beta_\xi = 1.95 \pm 0.05$ and $\beta_{m_1} = 1.81 \pm 0.03$, indicating a more prominent effect of transverse interaction at high strength for the self-breaking of grains from grain boundaries.

Grain Locomotion

The surface effect induced by net transverse interaction can be utilized to control the locomotion of individual odd crystalline grains, showing as migration or transport of grains with directional self-motion (either translation or rotation) even though the constituent particles are not self-propelled. This is achieved by imposing spatially varying transverse interaction strengths $\alpha_{j=0,1,2}$ in the T-PFC equation 2, which could correspond to spatial variation of individual particle spinning rates (as tuned by, e.g., rotating magnetic field applied to magnetic colloids, or similar avenues) that determine the magnitude of interparticle transverse force. It can be illustrated via an example of one-dimensional variation

$$\alpha_j(x) = \alpha_j^0 \cos Q_x(x - x_0), \quad (15)$$

where $j = 0, 1$ and $Q_x = 2\pi/\lambda_x$ with λ_x the spatial periodicity of α_j variation which can be controlled by, e.g., spatial dependence of magnetic field for spinning magnetic particles. This leads to a continuous transition across different modes of grain locomotion, as demonstrated in Fig. 5A and Movie S16 (where $\alpha_0 = \alpha_1$ and $\alpha_2 = 0$). When located at the minimum (with $\alpha_{j=0,1} < 0$) and maximum (with $\alpha_{j=0,1} > 0$) of the spatially varying $\alpha_j(x)$, the grain self-rotates clockwise (CW) and counterclockwise (CCW) respectively, with the maximum magnitude of rotation frequency ω but with the absence of translational motion. In contrast, when the grain is centered at $\alpha_j = 0$ with antisymmetric distribution of $\alpha_{j=0,1}$ in its two sides, pure self-translation occurs, without any grain rotation, and the grain self-travels along a path perpendicular to the direction of α_j variation. In between these two limits of modes, the grain locomotes via the combination of self-rotating and self-translating, i.e., a behavior of self-rolling, and the directions of motion (CW vs CCW rotation and $+y$ vs $-y$ translation) depends on the type of asymmetric distribution of $\alpha_{j=0,1}$ around the grain.

This transition between different locomotion modes can be understood via the microscopic picture of the corresponding surface transverse forces, as illustrated by the schematics in the middle panel of Fig. 5A. Note that nonzero net surface forces (or net surface odd stresses) are generated by the interparticle transverse interaction, as shown in the schematic of Fig. 1A. If the x -varying α_j distribution of transverse interaction strength is symmetric about the grain center, like the one located at the minimum of $\alpha_{j=0,1}$ (the leftmost schematic in the mid

panel of Fig. 5A), the net surface tangential forces generated at the opposite x -sides and opposite y -sides of the grain are of equal magnitude but opposite direction; thus there is no global translation force but a nonzero surface torque, leading to the behavior of pure self-rotation (CW in this case). When α_j increases, its asymmetric distribution along the x direction with respect to the grain center results in an unbalance of surface tangential forces on the opposite x -side surfaces, causing a nonzero global force pointed to the perpendicular y direction, together with the still nonzero but smaller net surface torque; this then leads to the behavior of self-rolling that combines $+y$ self-translation and slower CW self-rotation. A transition to the pure self-translation mode occurs when the grain center reaches $\alpha_j = 0$, for which α_j in two x -sides are of opposite sign and distribute antisymmetrically, such that net forces on the two x -side surfaces are equal in terms of both magnitude and direction, giving maximum translational motion but zero surface torque (no rotation). Further increasing α_j into the positive regime leads again to the unbalanced surface forces but CCW self-rotation, back to the phenomenon of self-rolling, until reaching the maximum location of α_j with its symmetric distribution across the grain and hence pure CCW self-rotation. The other half period of α_j variation follows the same microscopic mechanism, giving the self-traveling along the $-y$ direction and the variation from CCW to CW self-rotation, as seen in Fig. 5A and Movie S16.

As also shown in Fig. 5A, the time-average self-translation velocity $\langle v_c \rangle$ calculated at the steady state of simulations, with v_c the velocity of centroid (geometric center) of the grain, is well fitted to a form $\langle v_c \rangle = v_{c0} \sin Q_x(x - x_0)$, while the self-rotation frequency obeys $\langle \omega \rangle = \omega_0 \cos Q_x(x - x_0)$, with $\omega > 0$ for CCW rotation and $\omega < 0$ for CW rotation, in phase with α_j variation if compared to Eq. 15. This indicates a $\pi/2$ phase difference between grain self-translation and self-rotation, consistent with the above microscopic picture. It is noted that the behaviors of grain locomotion identified here are characterized by rigid-body self-motion of odd elastic crystallites, different from the usual scenarios of locomotion accompanied by body shape changes as being implemented recently in the adaptive locomotion of active metamaterials with odd elastic responses [54].

These results and the mechanism unveiled enable us to steer the locomotion or transport of grains along the desired paths. This can be achieved via the pre-designed 2D spatial distribution of transverse interaction strengths. Some simulation outcomes are presented in Fig. 5 B and C and Movies S17 and S18, for two examples of circular and S-shaped tracks for controlled locomotion. Here we approximate a kink-type α_j profile separating inner (with

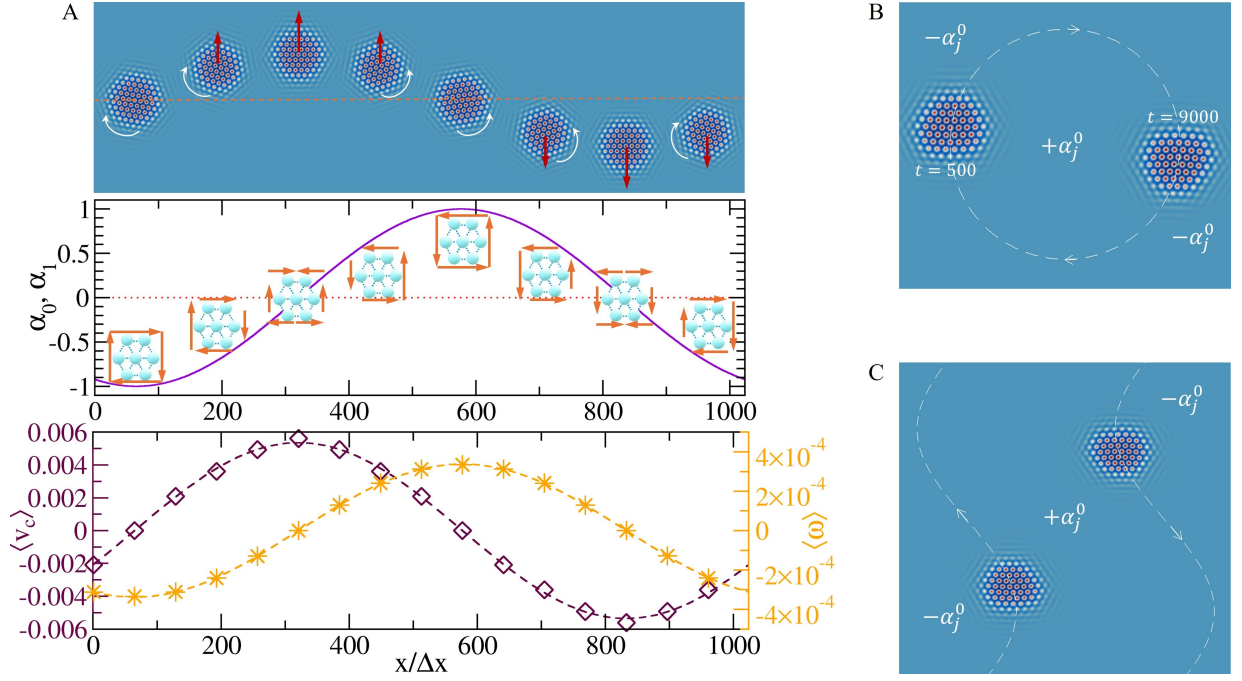


FIG. 5. Odd grain locomotion simulated via the T-PFC model. (A) A transition from self-rotation, self-rolling, to self-translation of grain locomotion as controlled via spatially-varying transverse interaction strength $\alpha_0 = \alpha_1$. The rotational and translational directions of the grain are indicated as arrows in the top panel which shows the simulation snapshot, the arrows in the middle panel illustrate the net surface transverse forces for each grain, and the spatial dependence of self-translation velocity $\langle v_c \rangle$ and self-rotation frequency $\langle \omega \rangle$ (averaged over $t = 3000$ – 5000) is given in the bottom panel, with dashed curves being the fitting to the data calculated from simulations. (B and C) The controlled transport of odd elastic grains along (B) a circular trajectory and (C) S-shaped tracks, through the pre-designed 2D spatial distribution of $\alpha_{j=0,1}$.

$\alpha_j = \alpha_j^{\text{in}}$) and outer (with $\alpha_j = \alpha_j^{\text{out}}$) domains as

$$\alpha_j(\mathbf{r}) = \frac{1}{2} (\alpha_j^{\text{out}} + \alpha_j^{\text{in}}) + \frac{1}{2} (\alpha_j^{\text{out}} - \alpha_j^{\text{in}}) \tanh\left(\frac{R_s(\mathbf{r})}{\Delta}\right), \quad (16)$$

where $R_s(\mathbf{r})$ is the signed distance function from position \mathbf{r} to the domain boundary (i.e., the boundary track for grain motion; see Materials and Methods) and Δ controls the boundary width. For simplicity we set $\alpha_j^{\text{in}} = -\alpha_j^{\text{out}} \equiv \alpha_j^0$, such that $\alpha_j = 0$ at the positions of boundary. When initialized with the grain center located at the boundary track, with $+/-$ antisymmetric α_j distribution across the boundary, the grain will self-travel by following the exact track that has been pre-designed, as seen in Fig. 5 and Movies S17 and S18. The direction of grain translation is always perpendicular to the local variation direction (i.e., spatial gradient) of transverse interaction strength α_j , based on the mechanism described above and illustrated in Fig. 5A. The maneuver of locomotion modes can be expected also from Fig. 5A, by placing the grain at an initial location deviated from the domain boundary, subjected to asymmetric distribution of α_j ; the grain will then locomote via self-rolling, as verified in our simulations.

CONCLUSIONS AND OUTLOOK

We have developed a multiscale density field theory, the T-PFC model incorporating microscopic and mesoscopic length scales and diffusive timescales, for the study of complex dynamical behaviors of 2D chiral crystalline systems that are governed by both longitudinal and transverse interactions. The model incorporates nonreciprocity, 2D parity symmetry breaking, and odd elasticity through new, lowest-order field-theoretical terms originated from transverse interactions. This nonpotential continuum-field model is validated by the study of odd crystallite self-rotation, dislocation self-motion, unbinding of dislocation dipoles instead of annihilation, and motion of grain boundaries, with results well agreeing with those observed in recent experiments and particle-based simulations of various systems formed by, e.g., starfish embryos, magnetic colloids, and swimming bacteria, and consistent with the microscopic picture of transverse forces.

Importantly, this modeling unveils a new type of surface cusp instability, which is the precursor of the subsequent surface dislocation nucleation and proliferation as well as the occurrence of self-fission or self-division of single-crystalline grains for strong enough transverse interaction. This behavior of grain self-fission leads to the prediction of

a transition from normal to reverse Ostwald ripening, and the spontaneous formation of a dynamical polycrystalline state with its governing dynamics transitioning from the normal grain coarsening to the persistently varying process of grain self-fragmentation as effects of transverse interaction become more prominent. The critical radius of grain instability and the characteristic grain sizes in the fragmentation-dominated regimes are found to obey power-law scaling behaviors with respect to the transverse interaction strength. Also achieved is grain locomotion without shape changes as effected by net transverse interactions on grain surface, with transition between different modes of self-rotating, self-rolling, and self-translating that are controlled via local spatial variation of transverse interaction strengths. The corresponding mechanism can be used to steer the transport of individual odd grain along designed trajectories that are either straight or curved, an intriguing feature for odd elastic systems.

The T-PFC model developed here constitutes a bridging between particle-based microscopic picture and continuum odd elasticity theory, enabling the simulations across a broad range of scales and system sizes that are of experimental relevance (ranging from a few to tens of thousands of particles), as demonstrated in the above calculations. Much larger systems can be simulated when needed, without losing particle resolution, through this T-PFC modeling and also the corresponding mesoscopic amplitude equations (Eqs. 5 and 6) as has been well demonstrated in previous PFC studies of passive systems. The modeling can be applied to examine and predict much more complex phenomena in chiral, odd crystalline systems that are beyond those presented here, such as mechanical and dynamical properties subjected to various external conditions, plastic deformation and dynamics of topological defects under variations of transverse interaction strengths, effects of confinements with different geometries and topologies, among many others. An interesting application for models of this type would be magnetic skyrmions, another example for a system with transverse interactions [55–57] and in particular odd elasticity [10]. In addition, the model is readily extended to the study of multicomponent mixtures with transverse interactions within the same and between different species, which are expected to generate a rich variety of complex dynamical behaviors and patterns as a result of coupling and competition between different degrees of freedom and multiple scales that can be well described by this PFC-type continuum approach.

MATERIALS AND METHODS

Numerical Simulations

The T-PFC model equation 2 or 3 is solved numerically via the pseudospectral method with the use of periodic

boundary conditions. The model parameters are chosen as $\epsilon = 0.1$, $g = 0.5$, $q_0 = 1$, and $\alpha_2 = 0$, with different values of α_1 and average density $\bar{\psi}_0$. When studying the cases with solid-liquid coexistence, $\bar{\psi}_0$ values in solid and liquid regions are chosen and adjusted according to the phase diagram calculated from original PFC [26] given that in one-mode approximation effects of transverse interaction can be neglected in the perfect bulk state. Sizes of simulated systems range from 512×512 to 2048×2048 grid points, with grid spacing $\Delta x = \Delta y = \pi/4$ and simulation time step $\Delta t = 0.5$ (with similar results obtained if using smaller Δt). Thus each system simulated for the study of multigrain dynamics in the polycrystalline state (of size 2048×2048 up to $t = 10^5$ as shown in Fig. 4) contains roughly 6.5×10^4 particles or density peaks.

For the study of grain locomotion, the simulated system size is set as 1024×512 grid points in Fig. 5A (with $\bar{\psi}_0|_{\text{solid}} = -0.076$ and $\bar{\psi}_0|_{\text{liquid}} = -0.116$) and 512×512 in Fig. 5 B and C (with $\bar{\psi}_0|_{\text{solid}} = -0.078$ and $\bar{\psi}_0|_{\text{liquid}} = -0.115$). The parameters used for the setup of α_j spatial variations are $\alpha_0^0 = \alpha_1^0 = 1$, $Q_x = 2\pi/L_x$ with $L_x = 1024\Delta x$, $x_0 = 9L_x/16$, and $\Delta = 8\Delta x$. For the circular trajectory shown in Fig. 5B, the signed distance function R_s in Eq. 16 of the corresponding $\alpha_j(\mathbf{r})$ profile is given by

$$R_s(\mathbf{r}) = |\mathbf{r} - \mathbf{r}_c| - r_0, \quad (17)$$

with center position \mathbf{r}_c and radius r_0 of the circle. For the S-shaped channel with two boundary tracks shown in Fig. 5C, the corresponding R_s in Eq. 16 is approximated by

$$R_s(\mathbf{r}) \approx |x - x_c| - [r_0 \mp S_0 \sin Q_s(y - y_c)], \quad (18)$$

where (x_c, y_c) is the location of the channel center, r_0 is the half width of the channel, S_0 and Q_s give the amplitude and wave number of the periodic S-shaped modulation, and “−” (“+”) is used for the region of $x > x_c$ ($x < x_c$). A variety of other types of α_j spatial profiles, with the corresponding boundary tracks set for different geometries or topologies, can be set up in a similar way through $R_s(\mathbf{r})$ (see, e.g., Ref. [40]).

ACKNOWLEDGMENTS

We thank Tzer Han Tan for providing the experimental data of Ref. [7] for cluster rotation frequencies of starfish embryos. Z.F.H. acknowledges support from the National Science Foundation under Grant No. DMR-2006446. M.t.V., R.W., and H.L. are funded by the Deutsche Forschungsgemeinschaft (DFG, German Research Foundation) – Project-IDs 465145163 – SFB 1552 (M.t.V.), 535275785 (R.W.), and LO 418/29-1 (H.L.).

-
- [1] L. Ratke and P. W. Voorhees, *Growth and Coarsening: Ostwald Ripening in Material Processing* (Springer, Berlin, 2002).
- [2] J. W. Cahn and J. E. Taylor, A unified approach to motion of grain boundaries, relative tangential translation along grain boundaries, and grain rotation, *Acta Mater.* **52**, 4887 (2004).
- [3] C. Qiu, M. Punke, Y. Tian, Y. Han, S. Wang, Y. Su, M. Salvalaglio, X. Pan, D. J. Srolovitz, and J. Han, Grain boundaries are brownian ratchets, *Science* **385**, 980 (2024).
- [4] M. Leoni and T. B. Liverpool, Dynamics and interactions of active rotors, *EPL* **92**, 64004 (2011).
- [5] Y. Fily, A. Baskaran, and M. C. Marchetti, Cooperative self-propulsion of active and passive rotors, *Soft Matter* **8**, 3002 (2012).
- [6] A. P. Petroff, X.-L. Wu, and A. Libchaber, Fast-moving bacteria self-organize into active two-dimensional crystals of rotating cells, *Phys. Rev. Lett.* **114**, 158102 (2015).
- [7] T. H. Tan, A. Mietke, J. Li, Y. Chen, H. Higinbotham, P. J. Foster, S. Gokhale, J. Dunkel, and N. Fakhri, Odd dynamics of living chiral crystals, *Nature* **607**, 287 (2022).
- [8] E. S. Bililign, F. B. Usabiaga, Y. A. Ganan, A. Poncet, V. Soni, S. Magkiriadou, M. J. Shelley, D. Bartolo, and W. T. M. Irvine, Motile dislocations knead odd crystals into whorls, *Nat. Phys.* **18**, 212 (2022).
- [9] C. Scheibner, A. Souslov, D. Banerjee, P. Surówka, W. Irvine, and V. Vitelli, Odd elasticity, *Nat. Phys.* **16**, 475 (2020).
- [10] L. Braverman, C. Scheibner, B. VanSaders, and V. Vitelli, Topological defects in solids with odd elasticity, *Phys. Rev. Lett.* **127**, 268001 (2021).
- [11] A. Poncet and D. Bartolo, When soft crystals defy Newton's third law: Nonreciprocal mechanics and dislocation motility, *Phys. Rev. Lett.* **128**, 048002 (2022).
- [12] S. H. Choi, Z.-F. Huang, and N. Goldenfeld, Noise-driven odd elastic waves in living chiral active matter (2024), arXiv:2411.09615.
- [13] C. B. Caporusso, G. Gonnella, and D. Levis, Phase coexistence and edge currents in the chiral Lennard-Jones fluid, *Phys. Rev. Lett.* **132**, 168201 (2024).
- [14] L. Caprini and U. Marini Bettolo Marconi, Bubble phase induced by odd interactions in chiral systems, *J. Chem. Phys.* **162**, 161101 (2025).
- [15] S. Shankar and L. Mahadevan, Active hydraulics and odd elasticity of muscle fibres, *Nat. Phys.* **20**, 1501 (2024).
- [16] M. J. Bowick, N. Fakhri, M. C. Marchetti, and S. Ramaswamy, Symmetry, thermodynamics, and topology in active matter, *Phys. Rev. X* **12**, 010501 (2022).
- [17] Z. You, A. Baskaran, and M. C. Marchetti, Nonreciprocity as a generic route to traveling states, *Proc. Natl. Acad. Sci. U.S.A.* **117**, 19767 (2020).
- [18] F. Brauns and M. C. Marchetti, Nonreciprocal pattern formation of conserved fields, *Phys. Rev. X* **14**, 021014 (2024).
- [19] S. Saha, J. Agudo-Canalejo, and R. Golestanian, Scalar active mixtures: The nonreciprocal Cahn-Hilliard model, *Phys. Rev. X* **10**, 041009 (2020).
- [20] G. Pisegna, S. Saha, and R. Golestanian, Emergent polar order in nonpolar mixtures with nonreciprocal interactions, *Proc. Natl. Acad. Sci. U.S.A.* **121**, e2407705121 (2024).
- [21] D. Greve, G. Lovato, T. Frohoff-Hülsmann, and U. Thiele, Coexistence of uniform and oscillatory states resulting from nonreciprocity and conservation laws, *Phys. Rev. Lett.* **134**, 018303 (2025).
- [22] Z.-F. Huang, M. te Vrugt, R. Wittkowski, and H. Löwen, Active pattern formation emergent from single-species nonreciprocity (2024), arXiv:2404.10093.
- [23] S. J. Kole, X. Chao, A. Mauleon-Amieva, R. Hanai, C. P. Royall, and T. B. Liverpool, Non-reciprocal interactions drive emergent chiral crystallites (2025), arXiv:2501.15996.
- [24] K. R. Elder, M. Katakowski, M. Haataja, and M. Grant, Modeling elasticity in crystal growth, *Phys. Rev. Lett.* **88**, 245701 (2002).
- [25] K. R. Elder, N. Provatas, J. Berry, P. Stefanovic, and M. Grant, Phase field crystal modeling and classical density functional theory of freezing, *Phys. Rev. B* **75**, 064107 (2007).
- [26] N. Provatas and K. R. Elder, *Phase Field Methods in Materials Science and Engineering* (Wiley-VCH, Weinheim, 2010).
- [27] P. Y. Chan, N. Goldenfeld, and J. Dantzig, Molecular dynamics on diffusive time scales from the phase-field-crystal equation, *Phys. Rev. E* **79**, 035701 (2009).
- [28] S. K. Mkhonta, K. R. Elder, and Z.-F. Huang, Exploring the complex world of two-dimensional ordering with three modes, *Phys. Rev. Lett.* **111**, 035501 (2013).
- [29] Z.-L. Wang, Z. R. Liu, and Z.-F. Huang, Angle-adjustable density field formulation for the modeling of crystalline microstructure, *Phys. Rev. B* **97**, 180102 (2018).
- [30] M. Salvalaglio and K. R. Elder, Coarse-grained modeling of crystals by the amplitude expansion of the phase-field crystal model: an overview, *Modelling Simul. Mater. Sci. Eng.* **30**, 053001 (2022).
- [31] H. Emmerich, H. Löwen, R. Wittkowski, T. Gruhn, G. I. Tóth, G. Tegze, and L. Gránágy, Phase-field-crystal models for condensed matter dynamics on atomic length and diffusive time scales: an overview, *Adv. Phys.* **61**, 665 (2012).
- [32] A. Adland, Y. Xu, and A. Karma, Unified theoretical framework for polycrystalline pattern evolution, *Phys. Rev. Lett.* **110**, 265504 (2013).
- [33] R. Backofen, K. Barmak, K. R. Elder, and A. Voigt, Capturing the complex physics behind universal grain size distributions in thin metallic films, *Acta Mater.* **64**, 72 (2014).
- [34] K. A. Moats, E. Asadi, and M. Laradji, Phase field crystal simulations of the kinetics of ostwald ripening in two dimensions, *Phys. Rev. E* **99**, 012803 (2019).
- [35] M. Salvalaglio, L. Angheluta, Z.-F. Huang, A. Voigt, K. R. Elder, and J. Viñals, A coarse-grained phase-field crystal model of plastic motion, *J. Mech. Phys. Solids* **137**, 103856 (2020).
- [36] M.-W. Liu, M. P. Gururajan, and K.-A. Wu, Morphological evolution of grain boundaries under lateral strains, *Phys. Rev. Mater.* **6**, 023601 (2022).
- [37] D. Burns, N. Provatas, and M. Grant, Two dimensional phase field crystal study of thermo-density coupling: Thermal expansion, recalescence, and plasticity, *Acta Mater.* **267**, 119712 (2024).
- [38] A. M. Menzel and H. Löwen, Traveling and resting crystals in active systems, *Phys. Rev. Lett.* **110**, 055702 (2013).

- [39] Z.-F. Huang, A. M. Menzel, and H. Löwen, Dynamical crystallites of active chiral particles, *Phys. Rev. Lett.* **125**, 218002 (2020).
- [40] Z.-F. Huang, H. Löwen, and A. Voigt, Defect dynamics in active smectics induced by confining geometry and topology, *Commun. Phys.* **5**, 294 (2022).
- [41] M. P. Holl, A. B. Steinberg, and U. Thiele, Motility-induced crystallization and rotating crystallites (2024), arXiv:2408.06114.
- [42] Z.-F. Huang, K. R. Elder, and N. Provatas, Phase-field-crystal dynamics for binary systems: Derivation from dynamical density functional theory, amplitude equation formalism, and applications to alloy heterostructures, *Phys. Rev. E* **82**, 021605 (2010).
- [43] J. Bickmann, S. Bröker, J. Jeggle, and R. Wittkowski, Analytical approach to chiral active systems: suppressed phase separation of interacting Brownian circle swimmers, *J. Chem. Phys.* **156**, 194904 (2022).
- [44] N. Goldenfeld, B. P. Athreya, and J. A. Dantzig, Renormalization group approach to multiscale simulation of polycrystalline materials using the phase field crystal model, *Phys. Rev. E* **72**, 020601 (2005).
- [45] K. R. Elder, Z.-F. Huang, and N. Provatas, Amplitude expansion of the binary phase-field-crystal model, *Phys. Rev. E* **81**, 011602 (2010).
- [46] R. Singh and M. E. Cates, Hydrodynamically interrupted droplet growth in scalar active matter, *Phys. Rev. Lett.* **123**, 148005 (2019).
- [47] J. S. Langer, Instabilities and pattern-formation in crystal growth, *Rev. Mod. Phys.* **52**, 1 (1980).
- [48] Z.-F. Huang, Scale-coupling and interface-pinning effects in the phase-field-crystal model, *Phys. Rev. E* **87**, 012401 (2013).
- [49] E. Tjhung, C. Nardini, and M. E. Cates, Cluster phases and bubbly phase separation in active fluids: reversal of the Ostwald process, *Phys. Rev. X* **8**, 031080 (2018).
- [50] C. H. Su and P. W. Voorhees, The dynamics of precipitate evolution in elastically stressed solids – I. Inverse coarsening, *Acta Mater.* **44**, 1987 (1996).
- [51] B. Liebchen and D. Levis, Collective behavior of chiral active matter: Pattern formation and enhanced flocking, *Phys. Rev. Lett.* **119**, 058002 (2017).
- [52] B. Zhang, A. Sokolov, and A. Snezhko, Reconfigurable emergent patterns in active chiral fluids, *Nat. Commun* **11**, 4401 (2020).
- [53] H. Massana-Cid, D. Levis, R. J. H. Hernández, I. Pagonabarraga, and P. Tierno, Arrested phase separation in chiral fluids of colloidal spinners, *Phys. Rev. Res.* **3**, L042021 (2021).
- [54] J. Veenstra, C. Scheibner, M. Brandenbourger, B. J., S. A., V. V., and C. C., Adaptive locomotion of active solids, *Nature* **639**, 935–941 (2025).
- [55] E. Kalz, H. D. Vuijk, J.-U. Sommer, R. Metzler, and A. Sharma, Oscillatory force autocorrelations in equilibrium odd-diffusive systems, *Phys. Rev. Lett.* **132**, 057102 (2024).
- [56] C. Reichhardt, C. J. O. Reichhardt, and M. V. Milošević, Statics and dynamics of skyrmions interacting with disorder and nanostructures, *Rev. Mod. Phys.* **94**, 035005 (2022).
- [57] K. Everschor-Sitte, J. Masell, R. M. Reeve, and M. Kläui, Perspective: Magnetic skyrmions—overview of recent progress in an active research field, *J. Appl. Phys.* **124** (2018).

Supporting Information for Anomalous grain dynamics and grain locomotion of odd crystals

Zhi-Feng Huang,¹ Michael te Vrugt,² Raphael Wittkowski,³ and Hartmut Löwen⁴

¹*Department of Physics and Astronomy, Wayne State University, Detroit, Michigan 48201, USA*

²*Institut für Physik, Johannes Gutenberg-Universität Mainz, 55128 Mainz, Germany*

³*Department of Physics, RWTH Aachen University; DWI – Leibniz Institute for Interactive Materials; 52074 Aachen, Germany*

⁴*Institut für Theoretische Physik II: Weiche Materie,
Heinrich-Heine-Universität Düsseldorf, 40225 Düsseldorf, Germany*

MODEL DERIVATION

Transverse interaction

We start from the microscopic equations of motion for N Brownian particles with transverse interactions. The i -th particle, located at position \mathbf{r}_i , undergoes overdamped motion and experiences, from the j -th particle, a conservative longitudinal force \mathbf{F}_{ij}^c and a nonconservative transverse force \mathbf{F}_{ij}^\perp . It is thereby governed by the Langevin equations

$$\dot{\mathbf{r}}_i(t) = \beta D_T \sum_{j \neq i} (\mathbf{F}_{ij}^c + \mathbf{F}_{ij}^\perp) + \sqrt{2D_T} \boldsymbol{\xi}_i, \quad (1)$$

where $\beta = 1/(k_B T)$ with Boltzmann constant k_B and temperature T is the thermodynamic beta, D_T is the translational diffusion coefficient, and $\boldsymbol{\xi}_i$ is a white noise with zero mean and unit variance. In two spatial dimensions (2D), the interparticle transverse force \mathbf{F}_{ij}^\perp is of the general form

$$\mathbf{F}_{ij}^\perp = f_{ij}^\perp \hat{\mathbf{z}} \times \frac{\mathbf{r}_{ij}}{r_{ij}}, \quad (2)$$

with the interparticle relative position vector $\mathbf{r}_{ij} = \mathbf{r}_i - \mathbf{r}_j$ and $r_{ij} = \|\mathbf{r}_{ij}\|$. We write the position vector as $\mathbf{r}_{ij} = r_{ij} \hat{\mathbf{u}}(\phi_R)$, where $\hat{\mathbf{u}}$ in 2D is parametrized via an angle ϕ_R in the form $\hat{\mathbf{u}} = (\cos(\phi_R), \sin(\phi_R))^T$. The transverse interaction force in Eq. 2 then reads

$$\mathbf{F}_{ij}^\perp = f^\perp(\mathbf{r}_i, \mathbf{r}_j, t) \begin{pmatrix} -\sin(\phi_R) \\ \cos(\phi_R) \end{pmatrix}. \quad (3)$$

Note that we allow here the force function f^\perp to explicitly depend on the positions of the two particles and on time, rather than only on their separation vector; i.e., it is possible that the transverse interaction has different magnitudes at different locations in space. This is exploited for the control of grain locomotion in the main text.

The Smoluchowski equation corresponding to the Langevin equations 1 is given by

$$\frac{\partial}{\partial t} \Psi = \sum_{i=1}^N \left[D_T \nabla_i^2 \Psi - \beta D_T \nabla_i \cdot (\mathbf{F}_{ij}^c \Psi) - \beta D_T \nabla_i \cdot (\mathbf{F}_{ij}^\perp \Psi) \right], \quad (4)$$

where $\Psi(\mathbf{r}_1, \dots, \mathbf{r}_N, t)$ is the N -body phase-space probability distribution function and ∇_i is the gradient operator with respect to the position vector \mathbf{r}_i . We define the one-body and two-body densities as

$$\rho(\mathbf{r}, t) = N \int d^2 r_2 \dots \int d^2 r_N \Psi(\mathbf{r}, \mathbf{r}_2, \dots, \mathbf{r}_N, t), \quad (5)$$

$$\rho^{(2)}(\mathbf{r}, t) = N(N-1) \int d^2 r_3 \dots \int d^2 r_N \Psi(\mathbf{r}, \mathbf{r}', \mathbf{r}_3, \dots, \mathbf{r}_N, t), \quad (6)$$

and write the conservative longitudinal force as

$$\mathbf{F}_{ij}^c = -\nabla_i U_2(\mathbf{r}_i - \mathbf{r}_j), \quad (7)$$

where U_2 is the interaction potential between two particles. Then, integrating Eq. 4 over the coordinates of all particles except for one gives

$$\frac{\partial}{\partial t} \rho(\mathbf{r}, t) = D_T \nabla^2 \rho(\mathbf{r}, t) + \beta D_T \nabla \cdot \left(\int d^2 r' \rho^{(2)}(\mathbf{r}, \mathbf{r}', t) \nabla U_2(\mathbf{r} - \mathbf{r}') \right) - \beta D_T \nabla \cdot \left(\int d^2 r' \rho^{(2)}(\mathbf{r}, \mathbf{r}', t) \mathbf{F}^\perp(\mathbf{r}, \mathbf{r}', t) \right). \quad (8)$$

The first two terms in Eq. 8 are standard and can be treated via the usual approximations of dynamical density functional theory. This procedure was outlined in Refs. [1, 2] and is not repeated here. It yields

$$\frac{\partial}{\partial t}\rho(\mathbf{r}, t) = \beta D_T \nabla \cdot \left(\rho(\mathbf{r}, t) \nabla \frac{\delta F}{\delta \rho(\mathbf{r}, t)} \right) - \beta D_T \nabla \cdot \left(\int d^2 r' \rho^{(2)}(\mathbf{r}, \mathbf{r}', t) \mathbf{F}^\perp(\mathbf{r}, \mathbf{r}') \right) \quad (9)$$

with the free energy functional F which will be specified later. For the remaining third term of Eq. 8, we make a mean-field approximation to get

$$\frac{\partial}{\partial t}\rho(\mathbf{r}, t) = \beta D_T \nabla \cdot \left(\rho(\mathbf{r}, t) \nabla \frac{\delta F}{\delta \rho(\mathbf{r}, t)} \right) - \beta D_T \nabla \cdot \left(\rho(\mathbf{r}, t) \int d^2 r' \left[\mathbf{F}^\perp(\mathbf{r}, \mathbf{r}', t) \rho(\mathbf{r}', t) \right] \right). \quad (10)$$

For the first term in Eq. 10, we make a lowest-order approximation via scaling analysis [3] that is equivalent to the constant mobility approximation [4]

$$\nabla \cdot \left(\rho(\mathbf{r}, t) \nabla \frac{\delta F}{\delta \rho(\mathbf{r}, t)} \right) \approx \rho_0 \nabla^2 \frac{\delta F}{\delta \rho(\mathbf{r}, t)}, \quad (11)$$

with a reference-state density ρ_0 . For the second term in Eq. 10, we remove the nonlocality via a gradient expansion [5]. Specifically, we make the substitution $\mathbf{r}' \rightarrow \mathbf{r} + \mathbf{r}'$ and use the gradient expansion [4, 6]

$$\rho(\mathbf{r} + \mathbf{r}', t) = \sum_{l=0}^{\infty} \frac{R^l}{l!} (u_j(\phi_R) \partial_j)^l \rho(\mathbf{r}, t), \quad (12)$$

where \mathbf{r} and $R = |\mathbf{r} - \mathbf{r}'|$ are separate variables, giving

$$\frac{\partial}{\partial t}\rho(\mathbf{r}, t) = \beta D_T \rho_0 \nabla^2 \frac{\delta F}{\delta \rho(\mathbf{r}, t)} + \sum_{l=0}^{\infty} \beta D_T \partial_i \left[\rho(\mathbf{r}, t) \int dR \int_0^{2\pi} d\phi_R \frac{R^{l+1}}{l!} f^\perp(\mathbf{r}, R, t) \epsilon_{ik} u_k(\phi_R) (u_j(\phi_R) \partial_j)^l \rho(\mathbf{r}, t) \right], \quad (13)$$

with summation over spatial indices appearing twice (i.e., the Einstein summation convention) and the 2D Levi-Civita symbol

$$\epsilon = \begin{pmatrix} 0 & 1 \\ -1 & 0 \end{pmatrix}. \quad (14)$$

In the following we will not write explicitly the dependence on \mathbf{r} and t unless needed. Integrating out Eq. 13 and truncating at $l = 5$ gives

$$\frac{\partial \rho}{\partial t} = D_T \left\{ \beta \rho_0 \nabla^2 \frac{\delta F}{\delta \rho} + \partial_i [\rho \epsilon_{ij} (A_1 \partial_j \rho + A_2 \partial_k^2 \partial_j \rho + A_3 (\partial_k^2)^2 \partial_j \rho)] \right\}, \quad (15)$$

with the coefficients

$$A_1(\mathbf{r}, t) = \pi \beta \int_0^\infty dR R^2 f^\perp(\mathbf{r}, R, t), \quad (16)$$

$$A_2(\mathbf{r}, t) = \frac{\pi}{8} \beta \int_0^\infty dR R^4 f^\perp(\mathbf{r}, R, t), \quad (17)$$

$$A_3(\mathbf{r}, t) = \frac{\pi}{192} \beta \int_0^\infty dR R^6 f^\perp(\mathbf{r}, R, t). \quad (18)$$

Note that the coefficients A_1, A_2, A_3 would be time and position dependent, i.e., $A_j = A_j(\mathbf{r}, t)$, in the case of spatially and/or temporally varying transverse force f^\perp . Since $\epsilon_{1j} \partial_j = \partial_y$ and $\epsilon_{2j} \partial_j = -\partial_x$, Eq. 15 can be rewritten as

$$\begin{aligned} \frac{\partial \rho}{\partial t} = D_T \left\{ \beta \rho_0 \nabla^2 \frac{\delta F}{\delta \rho} + [\partial_x(A_1 \rho)] \partial_y \rho - [\partial_y(A_1 \rho)] \partial_x \rho \right. \\ \left. + [\partial_x(A_2 \rho)] \partial_y \nabla^2 \rho - [\partial_y(A_2 \rho)] \partial_x \nabla^2 \rho + [\partial_x(A_3 \rho)] \partial_y \nabla^4 \rho - [\partial_y(A_3 \rho)] \partial_x \nabla^4 \rho \right\}, \end{aligned} \quad (19)$$

such that in 2D

$$\frac{\partial \rho}{\partial t} = D_T \left\{ \beta \rho_0 \nabla^2 \frac{\delta F}{\delta \rho} + [\nabla(A_1 \rho) \times \nabla \rho + \nabla(A_2 \rho) \times \nabla \nabla^2 \rho + \nabla(A_3 \rho) \times \nabla \nabla^4 \rho]_z \right\}. \quad (20)$$

If the $A_{j=1,2,3}$ coefficients are spatially constant, Eq. 20 simplifies to

$$\frac{\partial \rho}{\partial t} = D_T \left\{ \beta \rho_0 \nabla^2 \frac{\delta F}{\delta \rho} + [(\nabla \rho) \times \nabla (A_2 \nabla^2 \rho + A_3 \nabla^4 \rho)]_z \right\}. \quad (21)$$

The expressions of A_j depend on the specific form of transverse interaction. For example, if using the form of hydrodynamic near-field interaction force obtained from the lubrication theory, as applied to the study of chiral living crystals of starfish embryos [7], we have

$$f^\perp(r_{ij}) = \begin{cases} f_0 \ln\left(\frac{r_c}{r_{ij}-2r_0}\right), & \text{for } 2r_0 < r_{ij} < 2r_0 + r_c \\ 0, & \text{otherwise} \end{cases} \quad (22)$$

where r_0 is the radius of spinning particle and r_c sets the cutoff distance of the transverse force. Substituting Eq. 22 into Eqs. 16–18 leads to the explicit expressions

$$A_1 = \frac{\pi}{9} f_0 \beta r_c (36r_0^2 + 9r_0 r_c + r_c^2), \quad (23)$$

$$A_2 = \frac{\pi}{8} f_0 \beta \left(16r_0^4 r_c + 8r_0^3 r_c^2 + \frac{8r_0^2 r_c^3}{3} + \frac{r_0 r_c^4}{2} + \frac{r_c^5}{25} \right), \quad (24)$$

$$A_3 = \frac{\pi}{192} f_0 \beta \left(64r_0^6 r_c + 48r_0^5 r_c^2 + \frac{80r_0^4 r_c^3}{3} + 10r_0^3 r_c^4 + \frac{12r_0^2 r_c^5}{5} + \frac{r_0 r_c^6}{3} + \frac{r_c^7}{49} \right). \quad (25)$$

This is an example for the case where the A_j coefficients are spatially independent constants.

T-PFC model

For the free energy F , we use the simplest approximation that allows to model the crystalline phases, namely the phase field crystal (PFC) free energy functional F_{PFC} [8, 9]. This incorporates the effects of longitudinal interactions. The original form with one microscopic lattice length scale (of characteristic wave number Q_0) is given by [8]

$$F_{\text{PFC}} = \int d\mathbf{r} \left\{ \frac{1}{2} \phi \left[\Delta B + \lambda (\nabla^2 + Q_0^2)^2 \right] \phi - \frac{1}{3} \tau \phi^3 + \frac{1}{4} u \phi^4 \right\}, \quad (26)$$

and the corresponding conserved dynamics $D_T \nabla^2 \delta F_{\text{PFC}} / \delta \phi$ can be incorporated into Eq. 20. Similarly we could use other forms of F_{PFC} , such as those for multi-model PFC [10] or bond-angle dependent PFC [11] or others, to model a variety of crystalline lattice symmetries. Here, F_{PFC} corresponds to βF [3], and the density variation field $\phi = (\rho - \rho_0) / \rho_0$, with ρ_0 the reference-state density. From Eqs. 20 and 26 the model dynamics is governed by

$$\begin{aligned} \frac{\partial \phi}{\partial t} = D_T \left\{ \left[\nabla \left(\tilde{A}_1 (1 + \phi) \right) \times \nabla \phi + \nabla \left(\tilde{A}_2 (1 + \phi) \right) \times \nabla \nabla^2 \phi + \nabla \left(\tilde{A}_3 (1 + \phi) \right) \times \nabla \nabla^4 \phi \right]_z \right. \\ \left. + \nabla^2 \left[\Delta B \phi + \lambda (\nabla^2 + Q_0^2)^2 \phi - \tau \phi^2 + u \phi^3 \right] \right\}, \end{aligned} \quad (27)$$

where $\tilde{A}_j = \rho_0 A_j$ ($j = 1, 2, 3$). Setting $\tilde{\psi} = 1 + \phi = \rho / \rho_0$ leads to

$$\begin{aligned} \frac{\partial \tilde{\psi}}{\partial t} = D_T \left\{ \left[\nabla \left(\tilde{A}_1 \tilde{\psi} \right) \times \nabla \tilde{\psi} + \nabla \left(\tilde{A}_2 \tilde{\psi} \right) \times \nabla \nabla^2 \tilde{\psi} + \nabla \left(\tilde{A}_3 \tilde{\psi} \right) \times \nabla \nabla^4 \tilde{\psi} \right]_z \right. \\ \left. + \nabla^2 \left[\Delta B' \tilde{\psi} + \lambda (\nabla^2 + Q_0^2)^2 \tilde{\psi} - \tau' \tilde{\psi}^2 + u \tilde{\psi}^3 \right] \right\}, \end{aligned} \quad (28)$$

where $\Delta B' = \Delta B + 2\tau + 3u$ and $\tau' = \tau + 3u$.

Rescaling with respect to a length scale Q_0^{-1} , a time scale $(D_T \lambda Q_0^6)^{-1}$, and $\tilde{\psi} \rightarrow \sqrt{\lambda Q_0^4 / u} \psi$, we reach a dimensionless PFC equation incorporating transverse interaction (T-PFC)

$$\frac{\partial \psi}{\partial t} = \left[\nabla (\alpha_0 \psi) \times \nabla \psi + \nabla (\alpha_1 \psi) \times \nabla \nabla^2 \psi + \nabla (\alpha_2 \psi) \times \nabla \nabla^4 \psi \right]_z + \nabla^2 \left[-\epsilon \psi + (\nabla^2 + q_0^2)^2 \psi - g \psi^2 + \psi^3 \right], \quad (29)$$

where

$$\alpha_0 = \frac{\tilde{A}_1}{\sqrt{u\lambda Q_0^4}} = \frac{\rho_0}{\sqrt{u\lambda Q_0^2}} A_1, \quad \alpha_1 = \frac{Q_0^2 \tilde{A}_2}{\sqrt{u\lambda Q_0^4}} = \frac{\rho_0}{\sqrt{u\lambda}} A_2, \quad \alpha_2 = \frac{Q_0^4 \tilde{A}_3}{\sqrt{u\lambda Q_0^4}} = \frac{\rho_0 Q_0^2}{\sqrt{u\lambda}} A_3, \quad (30)$$

$$\epsilon = -\frac{\Delta B'}{\lambda Q_0^4} = -\frac{\Delta B + 2\tau + 3u}{\lambda Q_0^4}, \quad q_0 = 1, \quad g = \frac{\tau'}{\sqrt{u\lambda Q_0^2}} = \frac{\tau + 3u}{\sqrt{u\lambda Q_0^2}}, \quad \psi = \sqrt{\frac{u}{\lambda Q_0^4}} \tilde{\psi} = \sqrt{\frac{u}{\lambda}} \frac{\rho}{\rho_0 Q_0^2}. \quad (31)$$

Generally the transverse interaction strength $\alpha_{j=0,1,2}$ could vary with space and time, i.e., $\alpha_j = \alpha_j(\mathbf{r}, t)$. Equation 29 can be written as

$$\frac{\partial \psi}{\partial t} = -\nabla \cdot \mathbf{J} = -\nabla \cdot (\mathbf{J}_T + \mathbf{J}_{\text{PFC}}), \quad (32)$$

where the PFC flux $\mathbf{J}_{\text{PFC}} = -\nabla \mu_{\text{PFC}} = -\nabla \delta F_{\text{PFC}} / \delta \psi$ contributed by longitudinal interactions described in original PFC, and the flux generated by transverse interaction is given by (with $i, j = x, y$ here)

$$J_{T,i} = -\psi (\alpha_0 + \alpha_1 \nabla^2 + \alpha_2 \nabla^4) \epsilon_{ij} \partial_j \psi, \quad (33)$$

that is,

$$\mathbf{J}_T = -\psi (\alpha_0 + \alpha_1 \nabla^2 + \alpha_2 \nabla^4) \partial_y \psi \hat{x} + \psi (\alpha_0 + \alpha_1 \nabla^2 + \alpha_2 \nabla^4) \partial_x \psi \hat{y}. \quad (34)$$

In the case of spatially constant coefficients α_j , the T-PFC equation 29 is reduced to

$$\frac{\partial \psi}{\partial t} = [(\nabla \psi) \times \nabla (\alpha_1 \nabla^2 \psi + \alpha_2 \nabla^4 \psi)]_z + \nabla^2 [-\epsilon \psi + (\nabla^2 + q_0^2) \psi - g \psi^2 + \psi^3]. \quad (35)$$

The contribution from transverse interaction is presented as the first term of Eq. 35, which breaks the 2D parity symmetry (in terms of 2D parity inversion of $x \rightarrow -x$ or $y \rightarrow -y$), leading to 2D chirality. It is also antisymmetric with respect to the exchange of x and y .

MODEL ANALYSIS

One-mode approximation

Consider the one-mode approximation for a crystalline state governed by Eq. 35 with constant transverse interaction strength, i.e.,

$$\psi = \bar{\psi}_0 + \sum_j A_j^0 e^{i\mathbf{q}_j^0 \cdot \mathbf{r}} + \text{c.c.}, \quad (36)$$

where $\bar{\psi}_0$ is the average density variation and for a 2D hexagonal lattice structure with the steady-state selected wave number \tilde{q}_0 ($\sim q_0$), the basic wave vectors \mathbf{q}_j^0 ($j = 1, 2, 3$) are given by

$$\mathbf{q}_1^0 = \tilde{q}_0 \left(-\frac{\sqrt{3}}{2} \hat{x} - \frac{1}{2} \hat{y} \right), \quad \mathbf{q}_2^0 = \tilde{q}_0 \hat{y}, \quad \mathbf{q}_3^0 = \tilde{q}_0 \left(\frac{\sqrt{3}}{2} \hat{x} - \frac{1}{2} \hat{y} \right). \quad (37)$$

In the steady state of a perfect crystal the amplitudes A_j^0 are constant, and thus the corresponding one-mode expansion $(\partial_x \psi)(\partial_y \nabla^2 \psi) = (\partial_y \psi)(\partial_x \nabla^2 \psi) = -\tilde{q}_0^2 (\sum_j i q_{jx}^0 A_j^0 e^{i\mathbf{q}_j^0 \cdot \mathbf{r}} + \text{c.c.}) (\sum_k i q_{ky}^0 A_k^0 e^{i\mathbf{q}_k^0 \cdot \mathbf{r}} + \text{c.c.})$ and $(\partial_x \psi)(\partial_y \nabla^4 \psi) = (\partial_y \psi)(\partial_x \nabla^4 \psi) = \tilde{q}_0^4 (\sum_j i q_{jx}^0 A_j^0 e^{i\mathbf{q}_j^0 \cdot \mathbf{r}} + \text{c.c.}) (\sum_k i q_{ky}^0 A_k^0 e^{i\mathbf{q}_k^0 \cdot \mathbf{r}} + \text{c.c.})$, which leads to no contribution from the transverse terms, i.e., $[(\nabla \psi) \times \nabla (\alpha_1 \nabla^2 \psi + \alpha_2 \nabla^4 \psi)]_z = 0$ in one-mode approximation for a perfect crystalline state (it would be still nonzero in the presence of interface or defects when A_j^0 are not constant in space). This is consistent with the microscopic picture that inside a perfect crystal transverse interactions between atoms are balanced and thus do not affect the structure stability (at least to the lowest order), and the imbalance of transverse interactions would occur around the interfaces/boundaries or defects, as shown in the schematics of Fig. 1 of the main text. Also only transverse interactions (without longitudinal ones) cannot maintain the crystal structure, as can be seen in particle-based simulations [12] and also from Eqs. 35 and 36 that $d\bar{\psi}_0/dt = 0$ ($\bar{\psi}_0 = \text{const.}$) and $dA_j^0/dt = -D_T \tilde{q}_0^2 A_j^0$

(with a standard diffusion term $D_T \nabla^2 \rho$ but without the PFC terms), giving $A_j^0 \rightarrow 0$ at large time t , i.e., the dissolving of crystalline state.

Thus the one-mode solution for a perfect crystalline state of 2D hexagonal symmetry is the same as original PFC, with

$$A_j^0 \equiv A_0 = \frac{1}{15} \left\{ g - 3\bar{\psi}_0 \pm \sqrt{(g - 3\bar{\psi}_0)^2 - 15 [-\epsilon + (\tilde{q}_0^2 - q_0^2)^2 + 3\bar{\psi}_0^2 - 2g\bar{\psi}_0]} \right\}. \quad (38)$$

When $g - 3\bar{\psi}_0 > 0$, “+” sign is chosen with $A_0 > 0$, corresponding to a triangular lattice, while if $g - 3\bar{\psi}_0 < 0$, “-” sign is chosen with $A_0 < 0$, corresponding to a honeycomb lattice (i.e., inverse triangular, like graphene). The corresponding one-mode phase diagram is also the same as that of original PFC [8].

Amplitude equations for T-PFC

It would be useful to derive the amplitude equations for this T-PFC model, from which some analytic results can be better obtained, in addition to simulations at larger mesoscopic scales. In the amplitude expansion, the mesoscopic “slow” scales ($X = \varepsilon x, Y = \varepsilon y, T = \varepsilon t$) for ψ_0 and complex amplitudes A_j , with ε a dimensionless small parameter, are separated from the microscopic “fast” crystalline scales (x, y, t), such that

$$\psi = \psi_0(X, Y, T) + \sum_j A_j(X, Y, T) e^{i\mathbf{q}_j^0 \cdot \mathbf{r}} + \text{c.c.}, \quad (39)$$

with basic wave vectors \mathbf{q}_j^0 given in Eq. 37. Applying the procedure of amplitude formulation for the PFC model [3, 13] to Eq. 35, we obtain the amplitude equations for T-PFC (back to the original scales of (x, y, t) , with constant α_j coefficients) as

$$\begin{aligned} \frac{\partial \psi_0}{\partial t} = & [(\nabla \psi_0) \times \nabla (\alpha_1 \nabla^2 \psi_0 + \alpha_2 \nabla^4 \psi_0)]_z \\ & + \sum_j \{ [(\nabla + i\mathbf{q}_j^0) A_j] \times (\nabla - i\mathbf{q}_j^0) \}_z (\mathcal{G}_j^* - \tilde{q}_0^2) [\alpha_1 + \alpha_2 (\mathcal{G}_j^* - \tilde{q}_0^2)] A_j^* + \text{c.c.} \\ & + \nabla^2 \left[(-\epsilon + q_0^4) \psi_0 - g\psi_0^2 + \psi_0^3 + (6\psi_0 - 2g) \sum_j |A_j|^2 + 6(A_1 A_2 A_3 + \text{c.c.}) \right], \end{aligned} \quad (40)$$

$$\begin{aligned} \frac{\partial A_j}{\partial t} = & [(\nabla \psi_0) \times (\nabla + i\mathbf{q}_j^0)]_z (\mathcal{G}_j - \tilde{q}_0^2) [\alpha_1 + \alpha_2 (\mathcal{G}_j - \tilde{q}_0^2)] A_j + \{ [(\nabla + i\mathbf{q}_j^0) A_j] \times \nabla (\alpha_1 \nabla^2 \psi_0 + \alpha_2 \nabla^4 \psi_0) \}_z \\ & + \sum_{l \neq k \neq j} \{ [(\nabla - i\mathbf{q}_l^0) A_l^*] \times (\nabla - i\mathbf{q}_k^0) \}_z (\mathcal{G}_k^* - \tilde{q}_0^2) [\alpha_1 + \alpha_2 (\mathcal{G}_k^* - \tilde{q}_0^2)] A_k^* \\ & - \tilde{q}_0^2 \left[(-\epsilon + 3\psi_0^2 - 2g\psi_0) A_j + (\mathcal{G}_j - \tilde{q}_0^2 + q_0^2)^2 A_j + (6\psi_0 - 2g) \prod_{k \neq j} A_k^* + 3A_j \left(|A_j|^2 + 2 \sum_{k \neq j} |A_k|^2 \right) \right], \end{aligned} \quad (41)$$

where for the PFC terms (i.e., the last terms of Eqs. 40 and 41) we have used the long wavelength approximation as before [3, 14], and

$$\mathcal{G}_j = \mathcal{L}_j + \tilde{q}_0^2 = \nabla^2 + 2i\mathbf{q}_j^0 \cdot \nabla. \quad (42)$$

The last terms of Eqs. 40 and 41 can be rewritten as $\nabla^2 \delta \mathcal{F}_{\text{PFC}} / \delta \psi_0$ and $-\tilde{q}_0^2 \delta \mathcal{F}_{\text{PFC}} / \delta A_j^*$, respectively, with $\mathcal{F}_{\text{PFC}}[A_j, \psi_0]$ the effective PFC free energy functional given by [14]

$$\begin{aligned} \mathcal{F}_{\text{PFC}} = & \int d\mathbf{r} \left[(-\epsilon + 3\psi_0^2 - 2g\psi_0) \sum_j |A_j|^2 + \sum_j |(\mathcal{G}_j - \tilde{q}_0^2 + q_0^2) A_j|^2 + (6\psi_0 - 2g) \left(\prod_j A_j + \text{c.c.} \right) \right. \\ & \left. + \frac{3}{2} \sum_j |A_j|^4 + 6 \sum_{j < k} |A_j|^2 |A_k|^2 + \frac{1}{2} (-\epsilon + q_0^4) \psi_0^2 - \frac{1}{3} g \psi_0^3 + \frac{1}{4} \psi_0^4 \right]. \end{aligned} \quad (43)$$

Elastodynamics

It is important to examine whether this new T-PFC model with transverse interaction incorporates the property of odd elasticity. In the limit of small deformation with a displacement field \mathbf{u} varying slowly at long wavelength, when $\mathbf{r} \rightarrow \mathbf{r} + \mathbf{u}$ we have amplitudes $A_j \simeq A_j^0 \exp(-i\mathbf{q}_j^0 \cdot \mathbf{u})$, where in the steady state $\partial A_j^0 / \partial t = \partial \psi_0 / \partial t = 0$ and $\nabla A_j^0 = \nabla \psi_0 = 0$. To the first order of displacements $\mathcal{O}(\mathbf{u})$, the amplitude equations 40 and 41 give

$$\sum_j |A_j^0|^2 (\mathbf{q}_j^0 \times \nabla)_z [\alpha_1 + \alpha_2 (\mathcal{G}_j^* - 2\tilde{q}_0^2)] \mathcal{G}_j^* (\mathbf{q}_j^0 \cdot \mathbf{u}) = 0, \quad (44)$$

and

$$\begin{aligned} -iA_j^0 \frac{\partial}{\partial t} (\mathbf{q}_j^0 \cdot \mathbf{u}) &= \sum_{l \neq k \neq j} A_l^{0*} A_k^0 [\mathbf{q}_l^0 \times (\nabla - i\mathbf{q}_k^0)]_z [\alpha_1 + \alpha_2 (\mathcal{G}_k^* - 2\tilde{q}_0^2)] \mathcal{G}_k^* (\mathbf{q}_k^0 \cdot \mathbf{u}) \\ &\quad + i\tilde{q}_0^2 A_j^0 [\mathcal{G}_j^2 - 2(\tilde{q}_0^2 - q_0^2) \mathcal{G}_j] (\mathbf{q}_j^0 \cdot \mathbf{u}) \\ &\quad - \tilde{q}_0^2 \left\{ \left[-\epsilon + (\tilde{q}_0^2 - q_0^2)^2 + 3\psi_0^2 - 2g\psi_0 \right] A_j^0 + (6\psi_0 - 2g) \prod_{k \neq j} A_k^{0*} + 3A_j^0 \left(|A_j^0|^2 + 2 \sum_{k \neq j} |A_k^0|^2 \right) \right\}. \end{aligned} \quad (45)$$

If assuming in the steady state of a crystalline lattice $A_j^0 \simeq A_0$ (i.e., the one-mode solution given in Eq. 38 so that the last line of Eq. 45 is approximately equal to zero), we can obtain the following conditions at $\mathcal{O}(\mathbf{u})$ by separating the real and imaginary parts of Eq. 44,

$$[\alpha_1 + \alpha_2 (\nabla^2 - 3\tilde{q}_0^2)] \nabla^2 (\partial_x u_y - \partial_y u_x) = 0, \quad (46)$$

$$[\alpha_1 + 2\alpha_2 (\nabla^2 - \tilde{q}_0^2)] (\partial_x^2 u_x - \partial_y^2 u_x - 2\partial_x \partial_y u_y) = 0. \quad (47)$$

Similarly, the real part of Eq. 45 leads to

$$\begin{aligned} A_0 \sum_{l \neq k \neq j} \left\{ (\mathbf{q}_l^0 \times \nabla)_z \left[[\alpha_1 + \alpha_2 (\nabla^2 - 2\tilde{q}_0^2)] \nabla^2 - 4\alpha_2 (\mathbf{q}_k^0 \cdot \nabla)^2 \right] \right. \\ \left. - 2(\mathbf{q}_l^0 \times \mathbf{q}_k^0)_z (\mathbf{q}_k^0 \cdot \nabla) [\alpha_1 + 2\alpha_2 (\nabla^2 - \tilde{q}_0^2)] \right\} (\mathbf{q}_k^0 \cdot \mathbf{u}) - 4\tilde{q}_0^2 (\mathbf{q}_j^0 \cdot \nabla) [\nabla^2 - (\tilde{q}_0^2 - q_0^2)] (\mathbf{q}_j^0 \cdot \mathbf{u}) = 0, \end{aligned} \quad (48)$$

and for the imaginary part,

$$\begin{aligned} \frac{\partial}{\partial t} (\mathbf{q}_j^0 \cdot \mathbf{u}) &= A_0 \sum_{l \neq k \neq j} \left\{ 2(\mathbf{q}_l^0 \times \nabla)_z (\mathbf{q}_k^0 \cdot \nabla) [\alpha_1 + 2\alpha_2 (\nabla^2 - \tilde{q}_0^2)] \right. \\ &\quad \left. + (\mathbf{q}_l^0 \times \mathbf{q}_k^0)_z \left[[\alpha_1 + \alpha_2 (\nabla^2 - 2\tilde{q}_0^2)] \nabla^2 - 4\alpha_2 (\mathbf{q}_k^0 \cdot \nabla)^2 \right] \right\} (\mathbf{q}_k^0 \cdot \mathbf{u}) \\ &\quad - \tilde{q}_0^2 \left[\nabla^4 - 2(\tilde{q}_0^2 - q_0^2) \nabla^2 - 4(\mathbf{q}_j^0 \cdot \nabla)^2 \right] (\mathbf{q}_j^0 \cdot \mathbf{u}). \end{aligned} \quad (49)$$

At $j = 2$ Eq. 48 gives

$$\begin{aligned} &-2A_0 [\alpha_1 + \alpha_2 (\nabla^2 - 3\tilde{q}_0^2)] \nabla^2 \partial_y u_x + \alpha_2 A_0 \tilde{q}_0^2 \partial_x [6\partial_x \partial_y u_x + (\partial_x^2 + 3\partial_y^2) u_y] \\ &+ \frac{3}{2} A_0 \tilde{q}_0^2 [\alpha_1 + 2\alpha_2 (\nabla^2 - \tilde{q}_0^2)] (\partial_x u_y + \partial_y u_x) - 4\tilde{q}_0^2 [\nabla^2 - (\tilde{q}_0^2 - q_0^2)] \partial_y u_y = 0, \end{aligned} \quad (50)$$

where Eq. 46 has been used. Adding expressions of Eq. 48 at $j = 1$ and $j = 3$ and also with Eq. 50 yields

$$[\nabla^2 - (\tilde{q}_0^2 - q_0^2)] (\partial_x u_x + \partial_y u_y) = 0. \quad (51)$$

Subtracting between expressions of Eq. 48 at $j = 1$ and $j = 3$ leads to

$$\begin{aligned} &-A_0 [\alpha_1 + \alpha_2 (\nabla^2 - 3\tilde{q}_0^2)] \nabla^2 (\partial_x u_x - \partial_y u_y) + \alpha_2 A_0 \tilde{q}_0^2 [2\partial_x^3 u_x + 3(\partial_x^2 - \partial_y^2) \partial_y u_y] \\ &+ \frac{3}{2} A_0 \tilde{q}_0^2 [\alpha_1 + 2\alpha_2 (\nabla^2 - \tilde{q}_0^2)] (\partial_x u_x - \partial_y u_y) - 2\tilde{q}_0^2 [\nabla^2 - (\tilde{q}_0^2 - q_0^2)] (\partial_x u_y + \partial_y u_x) = 0. \end{aligned} \quad (52)$$

From expressions of Eq. 49 at $j = 1$ and $j = 3$ we get

$$\begin{aligned} \frac{\partial u_x}{\partial t} = & A_0 \tilde{q}_0^2 \left\{ - [\alpha_1 + 2\alpha_2 (\nabla^2 - \tilde{q}_0^2)] [\partial_x \partial_y u_x + (\partial_x^2 + 2\partial_y^2) u_y] - \frac{3}{2} [\alpha_1 + \alpha_2 (\nabla^2 - 3\tilde{q}_0^2)] \nabla^2 u_y \right. \\ & \left. + 3\alpha_2 \tilde{q}_0^2 \partial_y (\partial_x u_x + \partial_y u_y) \right\} - \tilde{q}_0^2 [\nabla^4 - 2(\tilde{q}_0^2 - q_0^2) \nabla^2 - \tilde{q}_0^2 (3\partial_x^2 + \partial_y^2)] u_x + 2\tilde{q}_0^4 \partial_x \partial_y u_y, \end{aligned} \quad (53)$$

$$\begin{aligned} \frac{\partial u_y}{\partial t} = & A_0 \tilde{q}_0^2 \left\{ [\alpha_1 + 2\alpha_2 (\nabla^2 - \tilde{q}_0^2)] (3\partial_x^2 u_x - \partial_x \partial_y u_y) + \frac{3}{2} [\alpha_1 + \alpha_2 (\nabla^2 - 3\tilde{q}_0^2)] \nabla^2 u_x \right. \\ & \left. - 3\alpha_2 \tilde{q}_0^2 \partial_x (\partial_x u_x + \partial_y u_y) \right\} + 6\tilde{q}_0^4 \partial_x \partial_y u_x - \tilde{q}_0^2 [\nabla^4 - 2(\tilde{q}_0^2 - q_0^2) \nabla^2 - \tilde{q}_0^2 (3\partial_x^2 + \partial_y^2)] u_y, \end{aligned} \quad (54)$$

while at $j = 2$ we have

$$\begin{aligned} \frac{\partial u_y}{\partial t} = & A_0 \tilde{q}_0^2 \left\{ \frac{1}{2} [\alpha_1 + 2\alpha_2 (\nabla^2 - \tilde{q}_0^2)] (3\nabla^2 u_x + 4\partial_x \partial_y u_y) + \frac{3}{2} [\alpha_1 + \alpha_2 (\nabla^2 - 3\tilde{q}_0^2)] \nabla^2 u_x \right. \\ & \left. - 3\alpha_2 \tilde{q}_0^2 \partial_x (\partial_x u_x + \partial_y u_y) \right\} - \tilde{q}_0^2 [\nabla^4 - 2(\tilde{q}_0^2 - q_0^2) \nabla^2 - 4\tilde{q}_0^2 \partial_y^2] u_y. \end{aligned} \quad (55)$$

Using Eq. 47 it can be shown that the first term of Eqs. 54 and 55 is equal to each other at $\mathcal{O}(\mathbf{u})$, but the rest are different. These two equations then give the following condition at the first order of displacements

$$2\partial_x \partial_y u_x + (\partial_x^2 - \partial_y^2) u_y = 0. \quad (56)$$

To remove the above ambiguity for the dynamical equation of u_y , we note that at the limit of $\alpha_1 = \alpha_2 = 0$ one can return to the result of original PFC for regular, even elasticity (with the major symmetry of elastic constants $C_{ijkl} = C_{klij}$). We thus need to choose a form consistent with the symmetric results at that limit, which is obtained via multiplying Eq. 54 by 1/3 and Eq. 55 by 2/3 and adding them together, as done for original PFC. This gives

$$\begin{aligned} \frac{\partial u_y}{\partial t} = & A_0 \tilde{q}_0^2 \left\{ [\alpha_1 + 2\alpha_2 (\nabla^2 - \tilde{q}_0^2)] [(2\partial_x^2 + \partial_y^2) u_x + \partial_x \partial_y u_y] + \frac{3}{2} [\alpha_1 + \alpha_2 (\nabla^2 - 3\tilde{q}_0^2)] \nabla^2 u_x \right. \\ & \left. - 3\alpha_2 \tilde{q}_0^2 \partial_x (\partial_x u_x + \partial_y u_y) \right\} + 2\tilde{q}_0^4 \partial_x \partial_y u_x - \tilde{q}_0^2 [\nabla^4 - 2(\tilde{q}_0^2 - q_0^2) \nabla^2 - \tilde{q}_0^2 (\partial_x^2 + 3\partial_y^2)] u_y. \end{aligned} \quad (57)$$

Equations 53 and 57 constitute the linear elastodynamical equations for the displacement field, in the overdamped limit of a crystalline state incorporating both longitudinal and transverse interactions. It can be seen that as long as $\alpha_1 \neq 0$ and/or $\alpha_2 \neq 0$, these elastodynamical equations are no longer symmetric with respect to $x \leftrightarrow y$, and the corresponding dynamical matrix becomes non-Hermitian, indicating the property of nonreciprocity of the system. This is caused by the $x \leftrightarrow y$ antisymmetry of the α_1 and α_2 terms, as originating from the corresponding antisymmetric property in the T-PFC equation 35. The rest of terms representing effects of longitudinal interactions (i.e., terms from original PFC) are symmetric with respect to $x \leftrightarrow y$.

To be specific, consider the general form of elastodynamical equation for the displacement field u_j ($j = x, y$)

$$\Gamma \frac{\partial u_j}{\partial t} = \partial_i \sigma_{ij} = C_{ijkl} \partial_i \partial_k u_l, \quad (58)$$

which is the overdamped version of Cauchy's equation of motion. Here Γ is the drag or friction coefficient and in linear elasticity the stress tensor $\sigma_{ij} = C_{ijkl} \partial_k u_l$, with elasticity tensor C_{ijkl} . Matching Eqs. 53 and 57 with the form of Eq. 58 and to the lowest order neglecting the fourth-order gradients of u_x and u_y , we get

$$\begin{aligned} C_{1111} = C_{2222} = & \Gamma \tilde{q}_0^2 (5\tilde{q}_0^2 - 2q_0^2), & C_{1122} = C_{2211} = & \Gamma \tilde{q}_0^2 (2q_0^2 - \tilde{q}_0^2), \\ C_{1212} = C_{2121} = & C_{1221} = C_{2112} = & \Gamma \tilde{q}_0^2 (3\tilde{q}_0^2 - 2q_0^2), \end{aligned} \quad (59)$$

which are of the same form as the original PFC with even elasticity (for which $\tilde{q}_0^2 = q_0^2$ and $\Gamma = 3A_0^2$; see Ref. [15]). Effects of transverse interaction with nonzero α_1 or α_2 terms enter into the property of elasticity via extra elastic constants C_{ijkk} ($i \neq j$) and C_{iikl} ($k \neq l$). Since nonzero internal torques can be induced by transverse interaction (leading to the lack of angular momentum conservation), we could no longer assume the left minor symmetry for these elastic constants, so that $C_{ijkk} \neq C_{jikl}$ (and thus $\sigma_{ij} \neq \sigma_{ji}$ with $i \neq j$). Since the system still maintains global rotational invariance as shown in the T-PFC model equation 35 and there is no coupling to rotational degrees of freedom, as in Ref. [16] deformation dependence of the elastic response with right mirror symmetry $C_{iikl} = C_{iilk}$ can

be assumed. We then have

$$\begin{aligned}
C_{1112} = C_{1121} &= -\frac{1}{2}\Gamma A_0 \tilde{q}_0^2 (5\alpha_1 - 13\tilde{q}_0^2 \alpha_2), & C_{2221} = C_{2212} &= \frac{1}{2}\Gamma A_0 \tilde{q}_0^2 (5\alpha_1 - 13\tilde{q}_0^2 \alpha_2), \\
C_{1211} &= \frac{1}{2}\Gamma A_0 \tilde{q}_0^2 (7\alpha_1 - 23\tilde{q}_0^2 \alpha_2), & C_{2111} &= \frac{3}{2}\Gamma A_0 \tilde{q}_0^2 (\alpha_1 - \tilde{q}_0^2 \alpha_2), \\
C_{2122} &= -\frac{1}{2}\Gamma A_0 \tilde{q}_0^2 (7\alpha_1 - 23\tilde{q}_0^2 \alpha_2), & C_{1222} &= -\frac{3}{2}\Gamma A_0 \tilde{q}_0^2 (\alpha_1 - \tilde{q}_0^2 \alpha_2),
\end{aligned} \tag{60}$$

which violate both the major symmetry and left minor symmetry, i.e., $C_{ijkk} \neq C_{kkij}$, $C_{iikl} \neq C_{klij}$, and $C_{ijkk} \neq C_{jikk}$. It is noted that these elastic constants are antisymmetric with respect to $1 \leftrightarrow 2$ (i.e., the exchange of x and y), with $C_{iikl} = -C_{jjlk}$ and $C_{ijkk} = -C_{jill}$ ($i \neq j$, $k \neq l$), which can be attributed to the $x \leftrightarrow y$ antisymmetry of the contributions of transverse interaction as seen from the α_1 and α_2 terms in Eqs. 35, 53, and 57.

The lack of major symmetry indicates the incorporation of both even and odd elasticity, showing as

$$C_{iikl} = C_{iikl}^{(e)} + C_{iikl}^{(o)}, \quad C_{ijkk} = C_{ijkk}^{(e)} + C_{ijkk}^{(o)}, \tag{61}$$

containing regular, even elasticity components with major symmetry $C_{ijkl}^{(e)} = C_{klij}^{(e)}$ as well as odd elasticity components with antisymmetric elastic constants $C_{ijkl}^{(o)} = -C_{klij}^{(o)}$ as a result of transverse interaction. The explicit expressions are given by

$$\begin{aligned}
C_{1112}^{(e)} = C_{1211}^{(e)} &= \frac{1}{2}\Gamma A_0 \tilde{q}_0^2 (\alpha_1 - 5\tilde{q}_0^2 \alpha_2), & C_{1112}^{(o)} &= -C_{1211}^{(o)} = -3\Gamma A_0 \tilde{q}_0^2 (\alpha_1 - 3\tilde{q}_0^2 \alpha_2), \\
C_{1121}^{(e)} = C_{2111}^{(e)} &= -\frac{1}{2}\Gamma A_0 \tilde{q}_0^2 (\alpha_1 - 5\tilde{q}_0^2 \alpha_2), & C_{1121}^{(o)} &= -C_{2111}^{(o)} = -2\Gamma A_0 \tilde{q}_0^2 (\alpha_1 - 2\tilde{q}_0^2 \alpha_2), \\
C_{1222}^{(e)} = C_{2212}^{(e)} &= \frac{1}{2}\Gamma A_0 \tilde{q}_0^2 (\alpha_1 - 5\tilde{q}_0^2 \alpha_2), & C_{1222}^{(o)} &= -C_{2212}^{(o)} = -2\Gamma A_0 \tilde{q}_0^2 (\alpha_1 - 2\tilde{q}_0^2 \alpha_2), \\
C_{2122}^{(e)} = C_{2221}^{(e)} &= -\frac{1}{2}\Gamma A_0 \tilde{q}_0^2 (\alpha_1 - 5\tilde{q}_0^2 \alpha_2), & C_{2122}^{(o)} &= -C_{2221}^{(o)} = -3\Gamma A_0 \tilde{q}_0^2 (\alpha_1 - 3\tilde{q}_0^2 \alpha_2).
\end{aligned} \tag{62}$$

If using the basis of dilation, rotation, and two independent shear modes introduced in Ref. [16], i.e.,

$$\tau^0 = \begin{pmatrix} 1 & 0 \\ 0 & 1 \end{pmatrix}, \quad \tau^1 = \begin{pmatrix} 0 & -1 \\ 1 & 0 \end{pmatrix}, \quad \tau^2 = \begin{pmatrix} 1 & 0 \\ 0 & -1 \end{pmatrix}, \quad \tau^3 = \begin{pmatrix} 0 & 1 \\ 1 & 0 \end{pmatrix}, \tag{63}$$

we can obtain the same form of the corresponding elastic tensor as in the continuum odd elasticity theory [16]

$$C^{\alpha\beta} = \frac{1}{2} \tau_{ij}^\alpha C_{ijkl} \tau_{kl}^\beta = 2 \begin{pmatrix} B & 0 & 0 & 0 \\ A & 0 & 0 & 0 \\ 0 & 0 & \mu & K^o \\ 0 & 0 & -K^o & \mu \end{pmatrix}, \tag{64}$$

with the bulk modulus B , the shear modulus μ , the odd modulus A caused by nonzero internal torque (with the violation of left minor symmetry of elastic constants), and another odd modulus K^o representing the antisymmetric coupling of two independent shear modes. All of them can be expressed explicitly in terms of T-PFC parameters, i.e.,

$$\begin{aligned}
B &= \frac{1}{2} (C_{1111} + C_{1122}) = 2\Gamma \tilde{q}_0^4, & \mu &= \frac{1}{2} (C_{1111} - C_{1122}) = \Gamma \tilde{q}_0^2 (3\tilde{q}_0^2 - 2q_0^2), \\
A &= \frac{1}{2} (C_{2111} - C_{1211}) = -\Gamma A_0 \tilde{q}_0^2 (\alpha_1 - 5\tilde{q}_0^2 \alpha_2), & K^o &= C_{1112} = -\frac{1}{2} (C_{2111} + C_{1211}) = -\frac{1}{2}\Gamma A_0 \tilde{q}_0^2 (5\alpha_1 - 13\tilde{q}_0^2 \alpha_2).
\end{aligned} \tag{65}$$

The linear instability analysis can be conducted on the elastodynamical equations 53 and 57, or equivalently Eq. 58, giving a non-Hermitian dynamical matrix in terms of C_{ijkl} , as well as the same form of results for perturbation growth rate and exceptional point as those of continuum odd elasticity theory in Ref. [16], with details expressed by T-PFC parameters.

These analytic results (and the numerical results presented in the main text) indicate that the lowest-order α_1 term in T-PFC is sufficient to model all the important effects of odd elasticity and transverse interaction. This can be also justified from symmetry consideration, i.e., rotational invariance and 2D chirality with the breaking of parity symmetry, of the α_1 term in the T-PFC equation.

ADDITIONAL DISCUSSION OF SIMULATION RESULTS

Grain self-rotation

Results from both T-PFC simulations and experimental data of starfish embryo living crystals, as presented in Fig. 1B of the main text, show a power law scaling of $\omega \sim N^{-1}$, where ω and N are the self-rotation frequency and particle number of the odd crystallite, respectively. This can be understood by noting that the steady-state frequency $\omega = \tau_{\text{net}}/\zeta_R$ in the overdamped limit, where ζ_R is the rotational friction coefficient and τ_{net} is the self-generated torque on the surface of crystallite as a result of net surface transverse force $F_{\text{net}}^\perp \propto 2\pi R\alpha_1$ (given that interparticle transverse forces cancel out in the bulk of a perfect lattice), i.e., $\tau_{\text{net}} = \int_s R dF_{\text{net}}^\perp \propto R^2\alpha_1$ for a surface of 2D grain with radius R . To estimate the R -dependence of ζ_R in 2D, consider a disk-shaped cluster of N particles, with area $\pi R^2 \propto N$. Each particle i inside has a velocity v_i and a translational friction coefficient γ_f (same for all particles), subjected to the friction force $f_i = -\gamma_f v_i$. In the case of translation of the cluster, $v_i \equiv v_0$ for all particles, and thus the total friction force of the cluster is $F_\gamma = \sum_{i=1}^N f_i = -N\gamma_f v_0 \propto -R^2\gamma_f v_0$. This leads to $\zeta_T \propto \gamma_f R^2$ in 2D, where ζ_T is the translational friction coefficient of the whole cluster. For the case of cluster rotation as addressed here, consider a ring within the cluster with a distance r from the center and a thickness dr . In the steady state with constant angular velocity ω_0 of the rotating cluster, the velocity of a particle i in this ring is $v_i = \omega_0 r$, so that the friction force for this ring of $dN \propto 2\pi r dr$ particles is given by $dF_\gamma = \gamma_f v_i dN \propto 2\pi\gamma_f\omega_0 r^2 dr$. Hence the total frictional torque corresponding to the rotation of the whole cluster is

$$M_\gamma = \int_0^R r dF_\gamma \propto - \int_0^R 2\pi\gamma_f\omega_0 r^3 dr = -\frac{\pi}{2}\gamma_f\omega_0 R^4, \quad (66)$$

leading to a scaling of the 2D rotational friction coefficient $\zeta_R \propto \gamma_f R^4$. Substituting this into the above overdamped result for the self-rotating grain gives

$$\omega = \tau_{\text{net}}/\zeta_R \propto (R^2\alpha_1)/R^4 = \alpha_1/R^2 \propto \alpha_1/N, \quad (67)$$

consistent with the scaling relation found in numerical simulations of T-PFC and the fitting to experimental data.

Surface cusp instability

The onset of surface cusp instability of self-rotating odd crystallites is found to obey a power-law scaling of $R_c \sim |\alpha_1|^{-2.5}$ from T-PFC simulation results shown in Fig. 2 of the main text, where R_c is the critical radius for the occurrence of grain instability. Here we show that the standard method of energy minimization is no longer valid for estimating the scaling behavior of this threshold radius R_c , which further demonstrates the large degree of deviation between the out-of-equilibrium, nonpotential system studied here and the near-equilibrium, potential counterparts. Consider a 2D crystalline area \mathcal{A} of totally \mathcal{N} grains, subjected to the constraint $\mathcal{N}\pi R^2 = \mathcal{A}$ with variable R and \mathcal{N} . If using the standard energetics argument, the rotating crystalline grains are assumed to be governed by a competition between surface line tension F_{surf} and the torsional elastic energy penalty F_{tor} . It has been known that [17] the torsional elastic energy density $f_{\text{tor}} = \frac{1}{2}C\vartheta_t^2$, where the torsional rigidity $C = \frac{1}{2}\pi\mu R^4$ (with shear modulus μ) for torsional deformation of a cylindrical rod. In the rod a circular cross section of radius R is twisted with respect to the adjoint one by a relative twist angle $d\phi$ and a torsion angle $\vartheta_t = d\phi/dz$ per unit rod length z . This can be matched to our case here, where a time series of rotating 2D circular grains can be considered as a time cylinder with each time cross section representing a circular grain state at that time and being rotated with respect to the grain state of the adjoint time step. Thus the rod length $z \rightarrow t$ and torsion angle $\vartheta_t = d\phi/dz \rightarrow \omega = d\phi/dt$, i.e., the rotation frequency with the relative rotation angle $d\phi$ between consecutive time sections. This leads to $f_{\text{tor}} = \frac{1}{4}\pi\mu\omega^2 R^4$ for a self-rotating circular grain with radius R . Note that the grain rotation rate ω increases with the net transverse force on the free surface and hence with the increase of α_1 , but decreases with larger grain size, i.e., $\omega \propto \alpha_1/N^s \sim \alpha_1/R^{2s}$ with $s > 0$. Results from both numerical simulations of T-PFC and experimental measurement of starfish embryos rotating clusters (with data obtained from Ref. [7]) show that $s \simeq 1$, as seen in Fig. 1B of the main text and Eq. 67. This yields $f_{\text{tor}} = C_0\alpha_1^2 R^{4-4s}$ where C_0 is proportional to the elastic modulus of the crystallite.

The total free energy of the crystalline grains is thus given by

$$F_g = F_{\text{bulk}} + F_{\text{surf}} + F_{\text{tor}} = \mathcal{N}(f_0\pi R^2 + \gamma_2\pi R + C_0\alpha_1^2 R^{4-4s}), \quad (68)$$

where f_0 is the bulk free energy density and γ is the 2D surface or line tension. The free energy variation of those self-rotating grains, $\Delta F_g = F_g - F_{\text{bulk}} = F_g - f_0 \mathcal{A}$, is then written as

$$\Delta F_g = \frac{2\mathcal{A}\gamma}{R} + \frac{\mathcal{A}C_0}{\pi} \alpha_1^2 R^{2-4s}, \quad (69)$$

the minimization of which gives the optimal grain radius in terms of energetics,

$$R_{\text{opt}} = \left[\frac{\pi\gamma}{C_0(1-2s)} \right]^{\frac{1}{3-4s}} |\alpha_1|^{-\frac{2}{3-4s}} \sim |\alpha_1|^{-\beta}. \quad (70)$$

Noting that due to the contribution of transverse interaction on the surface tangential force, γ would increase with α_1 (as seen in Ref. [18] for particle-based simulations of chiral fluid surface), we assume $\gamma \propto \alpha_1^\delta$ with $\delta > 0$. The scaling exponent for R_{opt} in Eq. 70 then becomes

$$\beta = \frac{2-\delta}{3-4s}. \quad (71)$$

Since there is no grain instability in the absence of transverse interaction, $R_{\text{opt}} \rightarrow \infty$ as $\alpha_1 \rightarrow 0$, such that $\beta > 0$. The positivity of grain radius imposes a constraint $s < 1/2$ in Eq. 70, giving a range of $0 < \beta < 2$. However, data fitting from both T-PFC simulations and starfish embryo experiments yields $s \simeq 1$, as described above and in the main text. In addition, a larger value of scaling exponent $\beta = 2.5 \pm 0.2$ is obtained from T-PFC simulations, with results shown in Fig. 2A of the main text. Both these indicate that the properties of this odd elastic system is not governed by energy minimization, as it is nonpotential and nonrelaxational.

-
- [1] A. J. Archer and R. Evans, Dynamical density functional theory and its application to spinodal decomposition, *J. Chem. Phys.* **121**, 4246 (2004).
 - [2] M. te Vrugt, H. Löwen, and R. Wittkowski, Classical dynamical density functional theory: from fundamentals to applications, *Adv. Phys.* **69**, 121 (2020).
 - [3] Z.-F. Huang, K. R. Elder, and N. Provatas, Phase-field-crystal dynamics for binary systems: Derivation from dynamical density functional theory, amplitude equation formalism, and applications to alloy heterostructures, *Phys. Rev. E* **82**, 021605 (2010).
 - [4] A. J. Archer, D. J. Ratliff, A. M. Rucklidge, and P. Subramanian, Deriving phase field crystal theory from dynamical density functional theory: consequences of the approximations, *Phys. Rev. E* **100**, 022140 (2019).
 - [5] A. J. M. Yang, P. D. Fleming, and J. H. Gibbs, Molecular theory of surface tension, *J. Chem. Phys.* **64**, 3732 (1976).
 - [6] M. te Vrugt, J. Bickmann, and R. Wittkowski, How to derive a predictive field theory for active Brownian particles: a step-by-step tutorial, *J. Phys.: Condens. Matter* **35**, 313001 (2023).
 - [7] T. H. Tan, A. Mietke, J. Li, Y. Chen, H. Higinbotham, P. J. Foster, S. Gokhale, J. Dunkel, and N. Fakhri, Odd dynamics of living chiral crystals, *Nature* **607**, 287 (2022).
 - [8] N. Provatas and K. R. Elder, *Phase Field Methods in Materials Science and Engineering* (Wiley-VCH, Weinheim, 2010).
 - [9] H. Emmerich, H. Löwen, R. Wittkowski, T. Gruhn, G. I. Tóth, G. Tegze, and L. Gránágy, Phase-field-crystal models for condensed matter dynamics on atomic length and diffusive time scales: an overview, *Adv. Phys.* **61**, 665 (2012).
 - [10] S. K. Mkhonta, K. R. Elder, and Z.-F. Huang, Exploring the complex world of two-dimensional ordering with three modes, *Phys. Rev. Lett.* **111**, 035501 (2013).
 - [11] Z.-L. Wang, Z. R. Liu, and Z.-F. Huang, Angle-adjustable density field formulation for the modeling of crystalline microstructure, *Phys. Rev. B* **97**, 180102 (2018).
 - [12] S. H. Choi, Z.-F. Huang, and N. Goldenfeld, Noise-driven odd elastic waves in living chiral active matter (2024), arXiv:2411.09615.
 - [13] N. Goldenfeld, B. P. Athreya, and J. A. Dantzig, Renormalization group approach to multiscale simulation of polycrystalline materials using the phase field crystal model, *Phys. Rev. E* **72**, 020601 (2005).
 - [14] Z.-F. Huang, Scale-coupling and interface-pinning effects in the phase-field-crystal model, *Phys. Rev. E* **87**, 012401 (2013).
 - [15] K. R. Elder, Z.-F. Huang, and N. Provatas, Amplitude expansion of the binary phase-field-crystal model, *Phys. Rev. E* **81**, 011602 (2010).
 - [16] C. Scheibner, A. Souslov, D. Banerjee, P. Surówka, W. Irvine, and V. Vitelli, Odd elasticity, *Nat. Phys.* **16**, 475 (2020).
 - [17] L. D. Landau and E. M. Lifshitz, *Theory of elasticity* (Pergamon, New York, 1970).
 - [18] C. B. Caporusso, G. Gonnella, and D. Levis, Phase coexistence and edge currents in the chiral Lennard-Jones fluid, *Phys. Rev. Lett.* **132**, 168201 (2024).